INTERNATIONAL JOURNAL FOR NUMERICAL METHODS IN FLUIDS
Int. J. Numer. Meth. Fluids 2007; **53**:1019–1048
Published online 20 September 2006 in Wiley InterScience (www.interscience.wiley.com). DOI: 10.1002/fld.1354

A higher-order Boussinesq-type model with moving bottom boundary: applications to submarine landslide tsunami waves

B. Ataie-Ashtiani*, † and A. Najafi Jilani‡

Department of Civil Engineering, Sharif University of Technology, Tehran, Iran

SUMMARY

A two-dimensional depth-integrated numerical model is developed using a fourth-order Boussinesq approximation for an arbitrary time-variable bottom boundary and is applied for submarine-landslide-generated waves. The mathematical formulation of model is an extension of (4,4) Padé approximant for moving bottom boundary. The mathematical formulations are derived based on a higher-order perturbation analysis using the expanded form of velocity components. A sixth-order multi-step finite difference method is applied for spatial discretization and a sixth-order Runge–Kutta method is applied for temporal discretization of the higher-order depth-integrated governing equations and boundary conditions. The present model is validated using available three-dimensional experimental data and a good agreement is obtained. Moreover, the present higher-order model is compared with fully potential three-dimensional models as well as Boussinesq-type multi-layer models in several cases and the differences are discussed. The high accuracy of the present numerical model in considering the nonlinearity effects and frequency dispersion of waves is proven particularly for waves generated in intermediate and deeper water area. Copyright © 2006 John Wiley & Sons, Ltd.

Received 24 April 2006; Revised 5 July 2006; Accepted 6 July 2006

KEY WORDS: submarine landslide; tsunami waves; impulsive waves; Boussinesq model; numerical model

1. INTRODUCTION

Tsunami waves may be generated by under water earthquakes, submarine landslides, rockslides or volcano explosions. Giant submerged landslides, normally in the form of debris avalanches, can produce impulsive waves and affect the entire coastline. Submarine-landslide-generated tsunamis

*Correspondence to: B. Ataie-Ashtiani, Department of Civil Engineering, Sharif University of Technology, Tehran, Iran.
†E-mail: ataie@sharif.edu
‡E-mail: najafi@sharif.edu

are one of the most hazardous phenomena that occur in the coastal areas. There are several approaches for mathematical formulation of water waves to simplify the real condition into two-dimensional horizontal domain. The main concern in different approaches is the accuracy of approximate equations to describe the nonlinearity effects and frequency dispersion of waves. A simple approach for water-wave simulation was developed based on non-linear shallow water (NSW) wave equations [1–6]. The results came from NSW improved in comparison with the results of simpler approaches such as linear or mild slope water wave equations but the wave frequency dispersion was not captured accurately [5].

As the next step and in order to increase the order of nonlinearity and dispersion, the Boussinesq-type models have been derived using polynomial approximation of the vertical profile of horizontal velocities. The classic Boussinesq equations were rewritten in depth-integrated form [7] assuming the second-order variation of velocity in vertical direction ((0,2) Padé approximant). In these equations, the nonlinearity and frequency dispersion of a wave are simulated in first and second orders, respectively [8–12]. Some researchers rearranged the second-order Boussinesq model in a new form to remove the spatial derivatives with an order higher than two to simplify the numerical simulation [13]. The comparison between numerical results and laboratory or field measurements shown that the main limitations of the NSW wave equations were improved, relatively, but the order of accuracy of wave dispersion simulation was not improved significantly [14, 15]. The wave heights after dispersion show significant deviation from measurements, particularly when the wave height exceeds 20% of wave's length. As an improvement in (0,2) Padé approximation of Boussinesq equations, some researchers rearranged the dispersive terms [3, 11, 16–19] or introduced a significant water depth, Z_α, as a characteristic water depth in which, the horizontal velocity domain is defined. In this (2,2) Padé approximant, the value of Z_α optimized using a least-square procedure aimed at minimizing errors in approximated waves phase speed [20, 21]. This technique improved the accuracy of depth-integrated second-order approaches but the main limitation was due to their nonlinearity and shoaling effects, particularly for high-amplitude waves [22]. This second-order one-layer approach involving Z_α was applied by some researches to study of submarine-landslide-generated waves [23] by rearrangement of the governing equations for a moving bottom boundary and the results were compared with lower-order Boussinesq-type models.

The extension of Boussinesq models to higher accuracy was continued by Gobbi *et al*. [24, 25]. They presented a (4,4) Padé approximant accurate to $O(\mu^4)$ for retaining terms in dispersion, and to all consequential orders in nonlinearity. They proved conclusively that the procedure of Nwogu [20] (i.e. definition of characteristic depth Z_α based on a least-square procedure) is necessarily not adequate for obtaining higher-order approximation. Thus, they defined a dependent variable as a weighted average of the velocity potential at two distinct water depths. They used the higher-order approximation in fixed bottom and a major improvement over the second-order models was found at least in one horizontal direction. The researches on extending the range of Boussinesq models to higher accuracy were continued by Lynett and Liu multi-layer approach [26]. They developed a set of model equations based on piecewise integration of the primitive equations through several arbitrary layers (two-layer in the study of submarine-landslide waves) within each layer, an independent velocity profile is derived which allows for achieving a higher-order accuracy while in each layer the order of approximation is $O(\mu^2)$.

The main objective of this work is to develop a higher-order Boussinesq-type numerical model with a moving bottom boundary to study the landslide-generated waves, in order to accurately capture the nonlinear affects as well as the frequency dispersion of waves. We extend the (4,4) Padé approximation [24, 25] for an arbitrary moving bottom boundary in two horizontal dimensions.

DOI: 10.1002/fld

A numerical model is developed using finite difference method (FDM) in a higher-order scheme for spatial and temporal discretization of governing equations to capture the higher accuracy and mass conservation.

2. FOURTH-ORDER BOUSSINESQ-TYPE MODEL FOR MOVING BOTTOM BOUNDARY

In this section, we extend the second-order Boussinesq-type model of Lynett and Liu [23] to derive a two-horizontal fourth-order approximation in dispersion and all consequential orders in nonlinearity. The derivation procedure is also based on an extension of Gobbi [25] (4,4) Padé approximant that developed for fixed bottom boundary. The perturbation analysis is used based on the expansion of velocity components. A schematic of the computational domain and the main geometric parameters are shown in Figure 1. The dimensionless form of governing equations and boundary conditions in three-dimensional domain are described as [23]

$$\mu^2 \nabla \cdot \mathbf{u} + w_z = 0 \quad \text{on} \quad -h \leqslant z \leqslant \varepsilon \cdot \zeta \quad \text{(continuity equation)} \tag{1}$$

$$\mathbf{u}_t + \varepsilon \mathbf{u} \nabla \cdot \mathbf{u} + \frac{\varepsilon}{\mu^2} w \mathbf{u}_z = -\nabla p \quad \text{on}$$

$$-h \leqslant z \leqslant \varepsilon \cdot \zeta \quad \text{(momentum equation in two horizontal directions)} \tag{2}$$

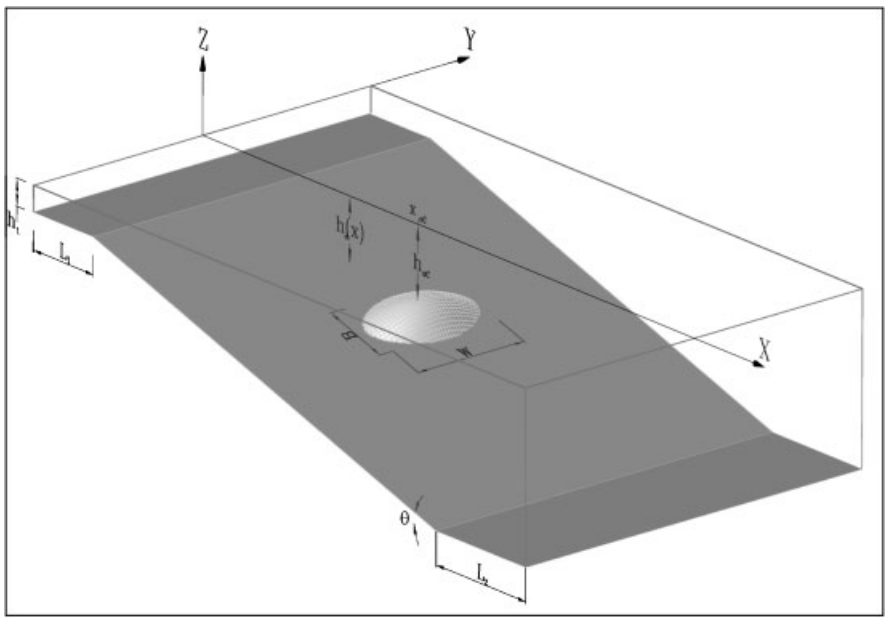

Figure 1. A schematic of numerical wave tank and basic parameters which used in mathematical formulation, the geometry of slide mass is described by Equation (52); the law of slide motion is described by Equations (53) and (54).

DOI: 10.1002/fld

$$\varepsilon w_t + \varepsilon^2 \mathbf{u} \cdot \nabla w + \frac{\varepsilon^2}{\mu^2} w w_z = -\varepsilon P_z - 1 \quad \text{on}$$

$$-h \leqslant z \leqslant \varepsilon \cdot \zeta \quad \text{(momentum equation in } z \text{ directions)} \tag{3}$$

$$w = \mu^2(\zeta_t + \varepsilon \cdot \mathbf{u} \cdot \nabla \zeta) \quad \text{on } z = \varepsilon \cdot \zeta \quad \text{(KFSBC)} \tag{4}$$

$$p = 0 \quad \text{on } z = \varepsilon \cdot \zeta \quad \text{(DFSBC)} \tag{5}$$

$$w + \mu^2 \mathbf{u} \cdot \nabla h + \frac{\mu^2}{\varepsilon} h_t = 0 \quad \text{on } z = -h \quad \text{(BBC)} \tag{6}$$

where x and y are the horizontal coordinates scaled by l_0 which is the horizontal length scale, z is the vertical coordinate scaled by h_0 which is the characteristic water depth, t is time and scaled by $l_0/(gh_0)^{1/2}$, ζ is the water surface displacement scaled by a_0 which is the impulse wave amplitude, h is the total depth based on still water considering the moving bottom boundary ($h(x, y, t)$) and scaled by h_0, $\mathbf{u}$ is the vector of horizontal velocity components (u, v) scaled by $\varepsilon \cdot (gh_0)^{1/2}$, w is the velocity in vertical direction scaled by $(\varepsilon/\mu) \cdot (gh_0)^{1/2}$, p is the water pressure scaled by γa_0, and $\nabla = (\partial/\partial x, \partial/\partial y)$ is the horizontal gradient vector.

The flow is considered to be irrotational. The irrotationality condition can be defined as

$$(w_y - v_z)\mathbf{i} + (w_x - u_z)\mathbf{j} + (v_x - u_y)\mathbf{k} = \mathbf{0} \tag{7}$$

and it yields the following equations in horizontal plane:

$$u_z = w_x \quad \text{and} \quad v_z = w_y \tag{8}$$

thus, we can derive the main irrotationality condition as

$$\mathbf{u}_z = \nabla w \tag{9}$$

The no-flow condition is assigned for lateral boundaries and the numerical simulation shall be stopped before the generated waves are received by lateral boundaries. The subscripts denote the partial derivative. The nonlinearity and dispersion parameters are $\varepsilon = a_0/h_0$ and $\mu = h_0/l_0$, respectively. In perturbation analysis, the velocity domain components '$\mathbf{u}$' and 'w' shall be expanded into [23]

$$\mathbf{u} = \mathbf{u}_0 + \mu^2 \mathbf{u}_1 + \mu^4 \mathbf{u}_2 \tag{10}$$

$$w = \mu^2 w_1 + \mu^4 w_2 \tag{11}$$

μ^2 is the basic small parameter in analysis. Substituting these expanded variables into dimensionless continuity equation (1) leads to

$$O(\mu^2) : \nabla \cdot \mathbf{u}_0 + w_{1z} = 0 \quad \text{on } -h \leqslant z \leqslant \varepsilon \cdot \zeta \tag{12}$$

$$O(\mu^4) : \nabla \cdot \mathbf{u}_1 + w_{2z} = 0 \quad \text{on } -h \leqslant z \leqslant \varepsilon \cdot \zeta \tag{13}$$

DOI: 10.1002/fld

Similarly, from moving seafloor boundary condition (6), it can be derived

$$O(\mu^2) : w_1 + \mathbf{u}_0 \cdot \nabla h + \frac{1}{\varepsilon} h_t = 0 \quad \text{on } z = -h \tag{14}$$

$$O(\mu^4) : w_2 + \mathbf{u}_1 \cdot \nabla h = 0 \quad \text{on } z = -h \tag{15}$$

On the other hand, substituting the expanded velocity components from Equations (10) and (11) into irrotational flow condition (i.e. Equation (9)), it can be derived [23]

$$\mathbf{u}_{0z} = \mathbf{0}, \quad \mathbf{u}_{1z} = \nabla w_1, \quad \mathbf{u}_{2z} = \nabla w_2 \tag{16}$$

From Equation (15) we can derive

$$w_1 = \int w_{1z}\, \mathrm{d}z = -\int \nabla \cdot \mathbf{u}_0\, \mathrm{d}z \tag{17}$$

Considering bottom boundary condition from Equation (14), the variable w_1 is obtained:

$$w_1 = -z\nabla \cdot \mathbf{u}_0 - \nabla \cdot (h\mathbf{u}_0) - \frac{1}{\varepsilon} h_t \tag{18}$$

From second-order irrotational flow condition (16), we can write

$$\mathbf{u}_1 = \int_{\tilde{z}}^{z} \mathbf{u}_{1z}\, \mathrm{d}z = \int_{\tilde{z}}^{z} \nabla w_1\, \mathrm{d}z \tag{19}$$

$\tilde{z}$ is the characteristic variable depth which is a weighted average of two distinct water depths which can be described in normalized form as: $\tilde{z} = [\beta \cdot z_a + (1-\beta) \cdot z_b]$. As shown conclusively by Gobbi *et al.* [25], z_a and z_b are the elevations that the horizontal velocity components are described and β is a weighting parameter which can be optimized in verification stage. Based on optimization of linear dispersion properties of fourth-order model, the characteristic depth z_a and z_b and the weighting parameter β can be described as [24, 25]

$$z_a = \left[\frac{1}{9} - \left\{\frac{8\beta}{567(1-\beta)}\right\}^{1/2} + \left\{\frac{\beta}{567\beta(1-\beta)}\right\}^{1/2}\right]^{1/2} - 1 \tag{20}$$

$$z_b = \left[\frac{1}{9} - \left\{\frac{8\beta}{567(1-\beta)}\right\}^{1/2}\right]^{1/2} - 1 \tag{21}$$

The variation range of β is between 0.018 and 0.467. In this work, the weighting parameter β is assumed 0.2 as recommended by Gobbi [25]. Thus, it can be derived from Equation (19):

$$\mathbf{u}_1 = -\tfrac{1}{2}(z^2 - \tilde{z}^2)\mathbf{A} - (z - \tilde{z})\nabla B \tag{22a}$$

where $\mathbf{A}$ is a two-component vector and B is a scalar and are defined as

$$\mathbf{A} = \nabla(\nabla \cdot \mathbf{u}_0), \quad B = \nabla \cdot (h\mathbf{u}_0) + \frac{1}{\varepsilon} h_t \tag{22b}$$

The higher-order terms of $\tilde{z}$ in normalized form describe as

$$\tilde{z}^n = \beta \cdot z_a^n + (1-\beta) \cdot z_b^n \tag{23}$$

DOI: 10.1002/fld

Now we repeat the above procedure for the next order (fourth order) of expanded variables (10, 11). From higher-order continuity equation (13) it can be obtained:

$$w_2 = \int w_{2z}\,\mathrm{d}z = -\int \nabla \mathbf{u}_1\,\mathrm{d}z \tag{24}$$

By substituting $\mathbf{u}_1$ from Equation (22a) and considering bottom boundary condition from Equation (15) for determination of integration coefficient as

$$w_2|_{z=-h} = -u_1|_{z=-h} \cdot \nabla h \tag{25}$$

it can be derived that

$$\begin{aligned} w_2 = {} & \tfrac{1}{6}z^3\nabla\cdot\mathbf{A} + \tfrac{1}{2}z^2\nabla\cdot(\nabla B) - \tfrac{1}{2}z\nabla\cdot(\tilde{z}^2\mathbf{A}) - z\nabla\cdot(\tilde{z}(\nabla B)) \\ & + \tfrac{1}{6}h^3\nabla\cdot\mathbf{A} - \tfrac{1}{2}h\nabla\cdot(\tilde{z}^2\cdot\mathbf{A}) + \tfrac{1}{2}h^2\nabla\cdot(\nabla B) - h\nabla\cdot(\tilde{z}(\nabla B)) \\ & + \tfrac{1}{2}h^2\mathbf{A}\cdot\nabla h - \tfrac{1}{2}\tilde{z}^2\mathbf{A}\cdot\nabla h - h\nabla h\cdot\nabla B - \tilde{z}\nabla h\cdot\nabla B \end{aligned} \tag{26}$$

Using irrotational flow condition defined in Equation (16), it can be derived that

$$\mathbf{u}_2 = \int_{\tilde{z}}^{z} \mathbf{u}_{2z}\,\mathrm{d}z = \int_{\tilde{z}}^{z} \nabla w_2\,\mathrm{d}z \tag{27}$$

Substituting w_2 from Equation (24) and considering characteristic water depth $\tilde{z}$, we have

$$\begin{aligned} \mathbf{u}_2 = {} & \tfrac{1}{24}(z^4-\tilde{z}^4)\nabla(\nabla\cdot\mathbf{A}) - \tfrac{1}{4}(z^2-\tilde{z}^2)\nabla(\nabla\cdot(\tilde{z}^2\cdot\mathbf{A})) + \tfrac{1}{6}(z^3-\tilde{z}^3)\nabla(\nabla\cdot(\nabla B)) \\ & - \tfrac{1}{2}(z^2-\tilde{z}^2)\nabla(\nabla\cdot(\tilde{z}(\nabla B))) + (z-\tilde{z})\cdot\nabla C \end{aligned} \tag{28}$$

where $\mathbf{A}$ and B are as defined in Equation (22b) and C is defined as

$$\begin{aligned} C = {} & \tfrac{1}{6}h^3\nabla\cdot\mathbf{A} - \tfrac{1}{2}h\nabla\cdot(\tilde{z}^2\mathbf{A}) + \tfrac{1}{2}h^2\nabla\cdot(\nabla B) - h\nabla\cdot(\tilde{z}(\nabla B)) + \tfrac{1}{2}h^2\mathbf{A}\cdot\nabla h \\ & - \tfrac{1}{2}\tilde{z}^2\cdot\mathbf{A}\cdot\nabla h - h\cdot\nabla h\cdot\nabla B - \tilde{z}\nabla h\cdot\nabla B \end{aligned} \tag{29}$$

We can substitute the variables w_1, $\mathbf{u}_1$, w_2 and $\mathbf{u}_2$ from Equations (18), (22a), (26) and (28) into (10) and (11) and obtain the expanded form of main variables $\mathbf{u}$ and w which are the velocity components in three-dimensional domain. For depth integration of domain equations, the expanded variables should be substituted into the z-direction momentum equation to derive the pressure distribution. Using Equation (3) and substituting expanded parameters from (10) and (11), it can be written as

$$\begin{aligned} P_z = {} & \frac{-1}{\varepsilon} + \mu^2(-w_{1t} - \varepsilon\mathbf{u}_0\cdot\nabla w_1 - \varepsilon w_1 w_{1z}) \\ & + \mu^4(-w_{2t} - \varepsilon\mathbf{u}_0\cdot\nabla w_2 - \varepsilon\mathbf{u}_1\cdot\nabla w_1 - \varepsilon w_1 w_{2z} - \varepsilon w_2 w_{1z}) + O(\mu^6) \end{aligned} \tag{30}$$

DOI: 10.1002/fld

By integrating the above equation from $\varepsilon\zeta$ to z, the water pressure at depth z can be obtained. Also the pressure in the $z=0$ can be derived from integration:

$$
\begin{aligned}
P|_{z=0} = {} & \zeta + \mu^2[-\tfrac{1}{2}\nabla\cdot\mathbf{u}_{0t}\varepsilon^2\zeta^2 + C_{1t}\varepsilon\zeta + \varepsilon\mathbf{u}_0\cdot(-\tfrac{1}{2}\nabla(\nabla\cdot\mathbf{u}_0)\varepsilon^2\zeta^2 + \varepsilon\zeta\nabla C_1) \\
& - \varepsilon\nabla\cdot\mathbf{u}_0\cdot(-\tfrac{1}{2}\varepsilon^2\zeta^2\nabla\cdot\mathbf{u}_0 + C_1\varepsilon\zeta)] \\
& + \mu^4[\tfrac{1}{24}\varepsilon^4\zeta^4\nabla\cdot\mathbf{A}_t + \tfrac{1}{6}\varepsilon^3\zeta^3\nabla\cdot(\nabla B_t) - \tfrac{1}{4}\varepsilon^2\zeta^2\nabla\cdot(\tilde{z}^2\mathbf{A})_t - \tfrac{1}{2}\varepsilon^2\zeta^2\nabla\cdot(\tilde{z}\nabla B)_t + \varepsilon\zeta C_t] \\
& + \mu^4\varepsilon\mathbf{u}_0\cdot[\tfrac{1}{24}\varepsilon^4\zeta^4\nabla(\nabla\cdot\mathbf{A}) + \tfrac{1}{6}\varepsilon^3\zeta^3\nabla(\nabla(\nabla B)) - \tfrac{1}{4}\varepsilon^2\zeta^2\nabla(\nabla\cdot(\tilde{z}^2\mathbf{A})) \\
& - \tfrac{1}{2}\varepsilon^2\zeta^2\nabla(\nabla\cdot(\tilde{z}\nabla B)) + \varepsilon\zeta\nabla C] \\
& + \mu^4\varepsilon[\tfrac{1}{8}\varepsilon^4\zeta^4\mathbf{A}\cdot\nabla(\nabla\cdot\mathbf{u}_0) - \tfrac{1}{4}\varepsilon^2\zeta^2\tilde{z}^2\mathbf{A}\cdot\nabla(\nabla\cdot\mathbf{u}_0) + \tfrac{1}{3}\varepsilon^3\zeta^3\nabla B\cdot\nabla(\nabla\cdot\mathbf{u}_0) \\
& - \tfrac{1}{2}\varepsilon^2\zeta^2\tilde{z}^2\nabla B\cdot\nabla(\nabla\cdot\mathbf{u}_0) - \tfrac{1}{6}\varepsilon^3\zeta^3\mathbf{A}\cdot\nabla C_1 + \tfrac{1}{2}\varepsilon\zeta\cdot\tilde{z}^2\mathbf{A}\cdot\nabla C_1 - \tfrac{1}{2}\varepsilon^2\zeta^2\nabla B\cdot\nabla C_1 \\
& + \varepsilon\zeta\cdot\tilde{z}^2\cdot\nabla B\cdot\nabla C_1 - \tfrac{1}{6}\varepsilon^3\zeta^3(\nabla\cdot\mathbf{A})(\nabla\cdot\mathbf{u}_0) - \tfrac{1}{3}\varepsilon^3\zeta^3(\nabla\cdot\mathbf{u}_0)(\nabla\cdot(\nabla B)) \\
& + \tfrac{1}{4}\varepsilon^2\zeta^2(\nabla\cdot\mathbf{u}_0)(\nabla\cdot(\tilde{z}^2\cdot\mathbf{A})) + \tfrac{1}{2}\varepsilon^2\zeta^2(\nabla\cdot\mathbf{u}_0)(\nabla\cdot(\tilde{z}\nabla B)) + \tfrac{1}{6}\varepsilon^3\zeta^3C_1(\nabla\cdot\mathbf{A}) \\
& + \tfrac{1}{2}\varepsilon^2\zeta^2C_1\nabla\cdot(\nabla B) - \tfrac{1}{2}\varepsilon\zeta C_1\nabla\cdot(\tilde{z}^2\mathbf{A}) - C_1\varepsilon\zeta\nabla\cdot(\tilde{z}\nabla B) \\
& - \tfrac{1}{2}\varepsilon\zeta C_1\nabla\cdot(\tilde{z}^2\mathbf{A}) - C_1\varepsilon\zeta\nabla\cdot(\tilde{z}\nabla B) - \tfrac{1}{24}\varepsilon^4\zeta^4(\nabla\cdot\mathbf{A})(\nabla\cdot\mathbf{u}_0) \\
& - \tfrac{1}{6}\varepsilon^3\zeta^3(\nabla\cdot\mathbf{u}_0)(\nabla\cdot(\nabla B)) \\
& + \tfrac{1}{4}\varepsilon^2\zeta^2(\nabla\cdot\mathbf{u}_0)(\nabla\cdot(\tilde{z}^2\mathbf{A})) + \tfrac{1}{2}\varepsilon^2\zeta^2(\nabla\cdot\mathbf{u}_0)(\nabla\cdot(\tilde{z}\cdot\nabla B)) - \varepsilon\zeta C\nabla\cdot\mathbf{u}_0] \qquad (31)
\end{aligned}
$$

where $C_1 = -B$ which defined in (22b).

Now we can obtain the main governing equations in the fourth-order depth-integrated form considering movable bottom boundary condition in two horizontal directions. Equation (1) is integrated from $z=-h$ to $z=\varepsilon\zeta$ to create the depth-integrated continuity equation.

$$
\nabla\cdot\left[\int_{-h}^{\varepsilon\zeta}\mathbf{u}\,\mathrm{d}z\right] + \frac{1}{\varepsilon}h_t + \zeta_t = 0 \qquad (32)
$$

The horizontal velocity vector $\mathbf{u}$ in the above equation can be replaced by its fourth-order expanded form which is presented in (10) using $\mathbf{u}_1$ and $\mathbf{u}_2$ variables obtained from (22a) and (28). Thus, higher-order ($O(\varepsilon^6, \mu^6)$ in truncated terms) continuity equation in depth-integrated form is obtained. Equation (33) is the first main equation that is solved by the other two horizontal

DOI: 10.1002/fld

momentum equations in the presented numerical model.

$$\begin{aligned}
&\frac{1}{\varepsilon}h_t + \zeta_t + \nabla\cdot\{(\varepsilon\zeta + h)\mathbf{u}_0 \\
&\quad + \mu^2[\tfrac{-1}{6}(\varepsilon^3\zeta^3 + h^3)\mathbf{A} + \tfrac{1}{2}\tilde{z}^2(\varepsilon\zeta + h)\mathbf{A} - \tfrac{1}{2}(\varepsilon^2\zeta^2 - h^2)(\nabla\cdot B) + \tilde{z}^2(\varepsilon\zeta + h)(\nabla\cdot B)] \\
&\quad + \mu^4[\tfrac{1}{120}(\varepsilon^5\zeta^5 + h^5)\nabla(\nabla\cdot\mathbf{A}) - \tfrac{1}{24}(\varepsilon\zeta + h)\tilde{z}^4\nabla(\nabla\cdot\mathbf{A}) - \tfrac{1}{12}(\varepsilon^3\zeta^3 + h^3)\nabla(\nabla\cdot(\tilde{z}^2\cdot\mathbf{A})) \\
&\quad + \tfrac{1}{4}(\varepsilon\zeta + h)\tilde{z}^2\nabla(\nabla\cdot(\tilde{z}^2\mathbf{A})) + \tfrac{1}{24}(\varepsilon^4\zeta^4 - h^4)\nabla(\nabla\cdot(\nabla B)) - \tfrac{1}{6}(\varepsilon\zeta + h)\tilde{z}^3\nabla(\nabla\cdot(\nabla B)) \\
&\quad - \tfrac{1}{6}(\varepsilon^3\zeta^3 + h^3)\nabla(\nabla\cdot(\tilde{z}\nabla B)) + \tfrac{1}{2}(\varepsilon\zeta + h)\tilde{z}\nabla(\nabla\cdot(\tilde{z}\nabla B)) \\
&\quad + \tfrac{1}{2}(\varepsilon^2\zeta^2 - h^2)\nabla C - (\varepsilon\zeta + h)\tilde{z}\nabla C]\} = O(\varepsilon^6, \mu^6)
\end{aligned} \tag{33}$$

The vector $\mathbf{A}$ and parameters B and C in the above equation are defined in Equations (22b) and (29), respectively. Similarly, the expanded forms of $\mathbf{u}$ and w and the water pressure in $z = 0$ presented in Equation (31) is replaced in horizontal momentum equation (2) to create the other two main governing equations. Thus, Equation (2) changes into

$$\begin{aligned}
&\mathbf{u}_{0t} + \varepsilon(\nabla\cdot\mathbf{u}_0)\mathbf{u}_0 + \varepsilon(w_1|_{z=0})\mathbf{u}_{0z} \\
&\quad + \mu^2[\mathbf{u}_{1t}|_{z=0} + \varepsilon(\nabla\cdot(\mathbf{u}_1|_{z=0}))\mathbf{u}_0 + \varepsilon(\nabla\cdot\mathbf{u}_0)(\mathbf{u}_1|_{z=0})\cdot + \varepsilon(w_2|_{z=0})\mathbf{u}_{0z} + (w_1|_{z=0})(\mathbf{u}_{1z}|_{z=0})] \\
&\quad + \mu^4[\mathbf{u}_{2t}|_{z=0} + \varepsilon(\nabla(\cdot\mathbf{u}_2|_{z=0}))\mathbf{u}_0 + \varepsilon(\nabla\cdot(\mathbf{u}_1|_{z=0}))(\mathbf{u}_1|_{z=0}) + \varepsilon(\nabla\cdot\mathbf{u}_0)(\mathbf{u}_2|_{z=0}) \\
&\quad + \varepsilon(w_2|_{z=0})(\mathbf{u}_{1z}|_{z=0}) + (w_1|_{z=0})(\mathbf{u}_{2z}|_{z=0})] \\
&\quad + \nabla(P|_{z=0}) = O(\varepsilon^6, \mu^6)
\end{aligned} \tag{34}$$

Equations (33) and (34) make a fully nonlinear and highly dispersive (FN-HD) equation set which describe the dispersion up to $O(\mu^6)$ and nonlinearity up to $O(\varepsilon^6)$ in truncated terms. If the bottom boundary condition assumed as a fixed arbitrary floor and $h_t = 0$, the above equations are identical to Equations (16) and (17) derived by Gobbi *et al.* [25]. These equations will be solved simultaneously to obtain the main three variables u, v (horizontal velocity components) and ζ (water wave elevation). A numerical model is developed using this set of equations to simulate the impulsive wave generation and propagation. The details of numerical method are discussed in the next section.

3. NUMERICAL MODEL

A numerical model is developed using finite difference method to solve the obtained fourth-order wave equations. A sixth-order multi-step scheme is selected to discrete the governing equations in

DOI: 10.1002/fld

a two-dimensional depth-integrated horizontal domain (2HD). Based on Equations (33) and (34), the maximum order of partial differential equations is five. Using Taylor's expansion, a sixth-order discretization scheme is developed. For instance, the discretized form for several orders of partial derivatives of the main variable $\mathbf{u}$ can be obtained as

$$\begin{aligned}
\frac{\partial \mathbf{u}}{\partial x} &= Gx1^n_{i,j}(u) \\
&= \frac{1}{24\Delta x}(18(\mathbf{u}_{i+1,j} - \mathbf{u}_{i-1,j}) - 3.6(\mathbf{u}_{i+2,j} - \mathbf{u}_{i-2,j}) \\
&\quad + 0.4(\mathbf{u}_{i+3,j} - \mathbf{u}_{i-3,j})) + O(\Delta x^6) \\
\frac{\partial^2 \mathbf{u}}{\partial x^2} &= Gx2^n_{i,j}(u) \\
&= \frac{1}{12\Delta x^2}(18(\mathbf{u}_{i+1,j} + \mathbf{u}_{i-1,j}) - 1.8(\mathbf{u}_{i+2,j} + \mathbf{u}_{i-2,j}) \\
&\quad + 0.4/3(\mathbf{u}_{i+3,j} + \mathbf{u}_{i-3,j}) - 97.6/3\mathbf{u}_{i,j}) + O(\Delta x^6) \\
\frac{\partial^3 \mathbf{u}}{\partial x^3} &= Gx3^n_{i,j}(u) \\
&= \frac{-1}{15.2\Delta x^3} \cdot (69.2/3(\mathbf{u}_{i+1,j} - \mathbf{u}_{i-1,j}) \\
&\quad - 40.7/3(\mathbf{u}_{i+2,j} - \mathbf{u}_{i-2,j}) + 1.2(\mathbf{u}_{i+3,j} - \mathbf{u}_{i-3,j}) \\
&\quad + 0.35/3(\mathbf{u}_{i+4,j} - \mathbf{u}_{i-4,j})) + O(\Delta x^6) \qquad (35) \\
\frac{\partial^4 \mathbf{u}}{\partial x^4} &= Gx4^n_{i,j}(u) \\
&= \frac{-3}{0.5\Delta x^4}(12.2/9(\mathbf{u}_{i+1,j} + \mathbf{u}_{i-1,j}) - 4.225/9(\mathbf{u}_{i+2,j} + \mathbf{u}_{i-2,j}) \\
&\quad + 0.2/3(\mathbf{u}_{i+3,j} + \mathbf{u}_{i-3,j}) - 0.04375/9(\mathbf{u}_{i+4,j} + \mathbf{u}_{i-4,j}) - 17.0625/9\mathbf{u}_{i,j}) + O(\Delta x^6) \\
\frac{\partial^5 \mathbf{u}}{\partial x^5} &= Gx5^n_{i,j}(u) \\
&= \frac{3}{256\Delta x^5} \cdot (5168/9(\mathbf{u}_{i+1,j} - \mathbf{u}_{i-1,j}) - 1664/3(\mathbf{u}_{i+2,j} - \mathbf{u}_{i-2,j}) \\
&\quad + 232(\mathbf{u}_{i+3,j} - \mathbf{u}_{i-3,j}) - 608/13.5(\mathbf{u}_{i+4,j} - \mathbf{u}_{i-4,j}) \\
&\quad + 104/27(\mathbf{u}_{i+5,j} - \mathbf{u}_{i-5,j})) + O(\Delta x^6)
\end{aligned}$$

DOI: 10.1002/fld

Similar scheme is used for other partial derivation in the main equation sets in both x- and y-directions. Based on this high-order finite difference scheme, the governing equations are discretized. For instance, the discretized form of Equation (33) can be derived as

$$\mathbf{Ax} = Gx2(u^n_{i,j}) + Gxy(v^n_{i,j}) \tag{36}$$

$$\mathbf{Ay} = Gxy(u^n_{i,j}) + Gy2(v^n_{i,j}) \tag{37}$$

$$B^n_{i,j} = Gx(h^n_{i,j} \cdot u^n_{i,j}) + Gy(h^n_{i,j} \cdot v^n_{i,j}) + \frac{1}{\varepsilon} \cdot \frac{h^{n+1}_{i,j} - h^n_{i,j}}{\Delta t} \tag{38}$$

$$\begin{aligned} C^n_{i,j} = {} & \tfrac{1}{6}(h^3)^n_{i,j} \cdot (Gx(\mathbf{Ax}) + Gy(\mathbf{Ay})) - \tfrac{1}{2}h^n_{i,j} \cdot (Gx((\tilde{z}^2)^n_{i,j} \cdot \mathbf{Ax}) + Gy((\tilde{z}^2)^n_{i,j} \cdot \mathbf{Ay})) \\ & + \tfrac{1}{2}(h^2)^n_{i,j}(Gx2(B^n_{i,j}) + Gy2(B^n_{i,j})) - h^n_{i,j} \cdot (Gx(\tilde{z}^n_{i,j} \cdot Gx(B^n_{i,j})) \\ & + Gy(\tilde{z}^n_{i,j} \cdot Gy(B^n_{i,j}))) + \tfrac{1}{2}(h^2)^n_{i,j}(\mathbf{Ax} \cdot Gx(h^n_{i,j}) + \mathbf{Ay} \cdot Gy(h^n_{i,j})) \\ & - \tfrac{1}{2}(\tilde{z}^2)^n_{i,j} \cdot (\mathbf{Ax} \cdot Gx(h^n_{i,j}) + \mathbf{Ay} \cdot Gy(h^n_{i,j})) - h^n_{i,j} \cdot (Gx(h^n_{i,j}) \cdot Gx(B^n_{i,j}) \\ & + Gy(h^n_{i,j}) \cdot Gy(B^n_{i,j})) - \tilde{z}^n_{i,j} \cdot (Gx(h^n_{i,j}) \cdot Gx(B^n_{i,j}) + Gy(h^n_{i,j}) \cdot Gy(B^n_{i,j})) \end{aligned} \tag{39}$$

Now parameters Rx and Ry can be defined as

$$\begin{aligned} Rx^n_{i,j} = {} & u^n_{0_{i,j}} \cdot (\varepsilon\zeta^n_{i,j} + h^n_{i,j}) + \mu^2 \cdot [\tfrac{-1}{6}\mathbf{Ax}(\varepsilon^3(\zeta^3)^n_{i,j} + (h^3)^n_{i,j}) + \tfrac{1}{2}\mathbf{Ax}(\tilde{z}^2)^n_{i,j} \cdot (\varepsilon\zeta^n_{i,j} + h^n_{i,j}) \\ & - \tfrac{1}{2}Gx(B^n_{i,j})(\varepsilon^2(\zeta^2)^n_{i,j} - (h^2)^n_{i,j}) + (\tilde{z})^n_{i,j}Gx(B^n_{i,j}) \cdot (\varepsilon\zeta^n_{i,j} + h^n_{i,j})] \\ & + \mu^4 \cdot [\tfrac{1}{120}(\varepsilon^5(\zeta^5)^n_{i,j} + (h^5)^n_{i,j}) \cdot Gx(GA^n_{i,j}) - \tfrac{1}{24}(\varepsilon\zeta^n_{i,j} + h^n_{i,j}) \cdot (\tilde{z}^4)^n_{i,j}Gx(GA^n_{i,j}) \\ & - \tfrac{1}{12}(\varepsilon^3(\zeta^3)^n_{i,j} + (h^3)^n_{i,j})Gx((\tilde{z}^2)^n_{i,j}GA^n_{i,j}) + \tfrac{1}{4}(\varepsilon\zeta^n_{i,j} + h^n_{i,j})(\tilde{z}^2)^n_{i,j}Gx((\tilde{z}^2)^n_{i,j}GA^n_{i,j}) \\ & + \tfrac{1}{24}(\varepsilon^4(\zeta^4)^n_{i,j} - (h^4)^n_{i,j})Gx(G2(B^n_{i,j})) - \tfrac{1}{6}(\varepsilon\zeta^n_{i,j} + h^n_{i,j})(\tilde{z}^3)^n_{i,j}Gx(G2(B^n_{i,j})) \\ & - \tfrac{1}{6}(\varepsilon^3(\zeta^3)^n_{i,j} + (h^3)^n_{i,j})(G2((\tilde{z})^n_{i,j}Gx(B^n_{i,j}))) \\ & + \tfrac{1}{2}(\varepsilon\zeta^n_{i,j} + h^n_{i,j})(\tilde{z})^n_{i,j}(G2((\tilde{z})^n_{i,j}Gx(B^n_{i,j}))) \\ & + \tfrac{1}{2}(\varepsilon^2\zeta^2 - h^2) \cdot Gx(C^n_{i,j}) - (\varepsilon\zeta + h)\tilde{z}Gx(C^n_{i,j})] \end{aligned} \tag{40}$$

DOI: 10.1002/fld

and

$$
\begin{aligned}
Ry_{i,j}^n = {} & u_{0_{i,j}}^n \cdot (\varepsilon\zeta_{i,j}^n + h_{i,j}^n) + \mu^2 \cdot [\tfrac{-1}{6}\mathbf{Ay}(\varepsilon^3(\zeta^3)_{i,j}^n + (h^3)_{i,j}^n) + \tfrac{1}{2}\mathbf{Ay}(\tilde{z}^2)_{i,j}^n \cdot (\varepsilon\zeta_{i,j}^n + h_{i,j}^n) \\
& - \tfrac{1}{2}Gy(B_{i,j}^n)(\varepsilon^2(\zeta^2)_{i,j}^n - (h^2)_{i,j}^n) + (\tilde{z})_{i,j}^n Gy(B_{i,j}^n) \cdot (\varepsilon\zeta_{i,j}^n + h_{i,j}^n)] \\
& + \mu^4 \cdot [\tfrac{1}{120}(\varepsilon^5(\zeta^5)_{i,j}^n + (h^5)_{i,j}^n) \cdot Gy(GA_{i,j}^n) - \tfrac{1}{24}(\varepsilon\zeta_{i,j}^n + h_{i,j}^n) \cdot (\tilde{z}^4)_{i,j}^n Gy(GA_{i,j}^n) \\
& - \tfrac{1}{12}(\varepsilon^3(\zeta^3)_{i,j}^n + (h^3)_{i,j}^n)Gy((\tilde{z}^2)_{i,j}^n GA_{i,j}^n) + \tfrac{1}{4}(\varepsilon\zeta_{i,j}^n + h_{i,j}^n)(\tilde{z}^2)_{i,j}^n Gy((\tilde{z}^2)_{i,j}^n GA_{i,j}^n) \\
& + \tfrac{1}{24}(\varepsilon^4(\zeta^4)_{i,j}^n - (h^4)_{i,j}^n)Gy(G2(B_{i,j}^n)) - \tfrac{1}{6}(\varepsilon\zeta_{i,j}^n + h_{i,j}^n)(\tilde{z}^3)_{i,j}^n Gy(G2(B_{i,j}^n)) \\
& - \tfrac{1}{6}(\varepsilon^3(\zeta^3)_{i,j}^n + (h^3)_{i,j}^n)(G2((\tilde{z})_{i,j}^n Gy(B_{i,j}^n))) \\
& + \tfrac{1}{2}(\varepsilon\zeta_{i,j}^n + h_{i,j}^n)(\tilde{z})_{i,j}^n (G2((\tilde{z})_{i,j}^n Gy(B_{i,j}^n))) \\
& + \tfrac{1}{2}(\varepsilon^2\zeta^2 - h^2) \cdot Gy(C_{i,j}^n) - (\varepsilon\zeta + h)\tilde{z}Gy(C_{i,j}^n)]
\end{aligned} \tag{41}
$$

Now, the discrete form of depth-integrated continuity equation can be obtained using sixth-order Runge–Kutta (R-K) method for temporal discretization. The detail of derivation of sixth-order R-K method is provided in Appendix A. Using the present one-step, six-stage extended R-K method, the discrete form of depth-integrated continuity equation is concluded as

$$
\begin{aligned}
\zeta_{i,j}^S &= \zeta_{i,j}^n - \frac{1}{\varepsilon}(h_{i,j}^S - h_{i,j}^n) - 0.674197\Delta t \cdot [Gx(Rx_{i,j}^n) + Gy(Ry_{i,j}^n)] \\
\zeta_{i,j}^{2S} &= \zeta_{i,j}^n - \frac{1}{\varepsilon}(h_{i,j}^{2S} - h_{i,j}^S) - 0.674197\Delta t \cdot [Gx(Rx_{i,j}^S) + Gy(Ry_{i,j}^S)] \\
\zeta_{i,j}^{3S} &= \zeta_{i,j}^n - \frac{1}{\varepsilon}(h_{i,j}^{3S} - h_{i,j}^{2S}) - 0.941974\Delta t \cdot [Gx(Rx_{i,j}^{2S}) + Gy(Ry_{i,j}^{2S})] \\
\zeta_{i,j}^{4S} &= \zeta_{i,j}^n - \frac{1}{\varepsilon}(h_{i,j}^{4S} - h_{i,j}^{3S}) - 0.286400\Delta t \cdot [Gx(Rx_{i,j}^{3S}) + Gy(Ry_{i,j}^{3S})] \\
\zeta_{i,j}^{5S} &= \zeta_{i,j}^n - \frac{1}{\varepsilon}(h_{i,j}^{5S} - h_{i,j}^{4S}) - 0.246018\Delta t \cdot [Gx(Rx_{i,j}^{4S}) + Gy(Ry_{i,j}^{4S})] \\
\zeta_{i,j}^{n+1} &= \zeta_{i,j}^n - \frac{1}{\varepsilon}(h_{i,j}^{n+1} - h_{i,j}^{5S}) - \Delta t \cdot \{0.080939[Gx(Rx_{i,j}^n) + Gy(Ry_{i,j}^n)] \\
&\quad + 0.185235[Gx(Rx_{i,j}^S) + Gy(Ry_{i,j}^S)] \\
&\quad + 0.185235[Gx(Rx_{i,j}^{2S}) + Gy(Ry_{i,j}^{2S})] + 0.154226[Gx(Rx_{i,j}^{3S}) + Gy(Ry_{i,j}^{3S})] \\
&\quad + 0.196431[Gx(Rx_{i,j}^{4S}) + Gy(Ry_{i,j}^{4S})] + 0.197934[Gx(Rx_{i,j}^{5S}) + Gy(Ry_{i,j}^{5S})]\}
\end{aligned} \tag{42}
$$

DOI: 10.1002/fld

where $h_{i,j}^{iS} = h(x, y, t^n + \alpha_i \Delta t)$ and α_i for $i = 1$ to 5 are defined in Appendix A. Similar approach is applied for depth-integrated higher-order Boussinesq-type momentum equation (34) to derive the discrete form of other two governing equations. Substituting the variables w_1, $\mathbf{u}_1$, w_2, $\mathbf{u}_2$ and $P|_{z=0}$ from Equations (18), (22a), (26), (28) and (31) into (34) and rearrangement of concluded equation, the discrete form of two-component momentum equation can be determined as follows:

$$\mathbf{A}'\mathbf{x} = Gx2(Ax_{i,j}^n) + Gxy(Ay_{i,j}^n) \tag{43}$$

$$\mathbf{A}'\mathbf{y} = Gxy(Ax_{i,j}^n) + Gy2(Ay_{i,j}^n) \tag{44}$$

$$\mathbf{B}'\mathbf{x} = Gx3(B_{i,j}^n) + Gxy2(B_{i,j}^n) \tag{45}$$

$$\mathbf{B}'\mathbf{y} = Gyx2(B_{i,j}^n) + Gy3(B_{i,j}^n) \tag{46}$$

$$\begin{aligned} C'^n_{i,j} = {} & Gx(u_{i,j}^n) + Gy(v_{i,j}^n) + \mu^2[\tilde{z}_{i,j}^n \cdot (\mathbf{A}\mathbf{x} \cdot Gx(\tilde{z}_{i,j}^n) + \mathbf{A}\mathbf{y} \cdot Gy(\tilde{z}_{i,j}^n)) + \tfrac{1}{2}(\tilde{z}^2)_{i,j}^n (Gx(\mathbf{A}\mathbf{x}_{i,j}^n) \\ & + Gy(\mathbf{A}\mathbf{y}_{i,j}^n)) Gx(\tilde{z}_{i,j}^n) \cdot Gx(B_{i,j}^n) + Gy(\tilde{z}_{i,j}^n) \cdot Gy(B_{i,j}^n) + \tilde{z}_{i,j}^n \cdot (Gx2(B_{i,j}^n) + Gy2(B_{i,j}^n))] \\ & - \mu^4[\tfrac{1}{2}(\tilde{z}^3)_{i,j}^n \cdot (\mathbf{A}'\mathbf{x} \cdot Gx(\tilde{z}_{i,j}^n) + \mathbf{A}'\mathbf{y} \cdot Gy(\tilde{z}_{i,j}^n)) + \tfrac{1}{8}(\tilde{z}^4)_{i,j}^n (Gx(\mathbf{A}'\mathbf{x}_{i,j}^n) + Gy(\mathbf{A}'\mathbf{y}_{i,j}^n)) \\ & + \tfrac{1}{2}\tilde{z}_{i,j}^n \cdot (\mathbf{B}'\mathbf{x} \cdot Gx(\tilde{z}_{i,j}^n) + \mathbf{B}'\mathbf{y} \cdot Gy(\tilde{z}_{i,j}^n)) + \tfrac{1}{6}(\tilde{z}^3)_{i,j}^n \cdot (Gx(\mathbf{B}'\mathbf{x}_{i,j}^n) + Gy(\mathbf{B}'\mathbf{y}_{i,j}^n))] \end{aligned} \tag{47}$$

$$\begin{aligned} D_{i,j}^n = {} & \mu^2(-B_{i,j}^n) + \mu^4(\tfrac{1}{3}(\tilde{z}^3)_{i,j}^n (Gx(\mathbf{A}\mathbf{x}_{i,j}^n) + Gy(\mathbf{A}\mathbf{y}_{i,j}^n)) \\ & + \tfrac{1}{2}(\tilde{z}^2)_{i,j}^n (Gx2(B_{i,j}^n) + Gy2(B_{i,j}^n))) \end{aligned} \tag{48}$$

$$\begin{aligned} R'x_{i,j}^n = {} & \varepsilon(C' \cdot u_{i,j}^n - D \cdot Gx(B_{i,j}^n)) + \mu^2[\tfrac{1}{2}\varepsilon C'(\tilde{z}^2)_{i,j}^n \mathbf{A}\mathbf{x} + \varepsilon C'\tilde{z}_{i,j}^n \cdot Gx(B_{i,j}^n) \\ & + \varepsilon \cdot D_{i,j}^n \cdot (\tfrac{1}{3}(\tilde{z}^3)_{i,j}^n \cdot \mathbf{A}'\mathbf{x} + \tfrac{1}{2}(\tilde{z}^2)_{i,j}^n \cdot \mathbf{B}'\mathbf{x})] \\ & + \mu^4[-\tfrac{1}{8}\varepsilon C'(\tilde{z}^4)_{i,j}^n \mathbf{A}'\mathbf{x} - \tfrac{1}{6}\varepsilon C'(\tilde{z}^3)_{i,j}^n \mathbf{B}'\mathbf{x}] + Gx(P|_{z=0})_{i,j}^n \\ R'y_{i,j}^n = {} & \varepsilon(C' \cdot v_{i,j}^n - D \cdot Gy(B_{i,j}^n)) + \mu^2[\tfrac{1}{2}\varepsilon C'(\tilde{z}^2)_{i,j}^n \mathbf{A}\mathbf{y} + \varepsilon C'\tilde{z}_{i,j}^n \cdot Gy(B_{i,j}^n) \\ & + \varepsilon \cdot D_{i,j}^n \cdot (\tfrac{1}{3}(\tilde{z}^3)_{i,j}^n \cdot \mathbf{A}'\mathbf{y} + \tfrac{1}{2}(\tilde{z}^2)_{i,j}^n \cdot \mathbf{B}'\mathbf{y})] \\ & + \mu^4[-\tfrac{1}{8}\varepsilon C'(\tilde{z}^4)_{i,j}^n \mathbf{A}'\mathbf{y} - \tfrac{1}{6}\varepsilon C'(\tilde{z}^3)_{i,j}^n \mathbf{B}'\mathbf{y}] + Gy(P|_{z=0})_{i,j}^n \end{aligned} \tag{49}$$

DOI: 10.1002/fld

Using sixth-order R-K method, the discrete form of momentum equation in two horizontal dimensions can be derived as

$$
\begin{aligned}
u_{i,j}^{S} &= u_{i,j}^{n} - 0.674197\Delta t \cdot [(R' x_{i,j}^{n})] \\
u_{i,j}^{2S} &= u_{i,j}^{n} - 0.674197\Delta t \cdot [(R' x_{i,j}^{S})] \\
u_{i,j}^{3S} &= u_{i,j}^{n} - 0.941974\Delta t \cdot [(R' x_{i,j}^{2S})] \\
u_{i,j}^{4S} &= u_{i,j}^{n} - 0.286400\Delta t \cdot [(R' x_{i,j}^{3S})] \\
u_{i,j}^{5S} &= u_{i,j}^{n} - 0.246018\Delta t \cdot [(R' x_{i,j}^{4S})] \\
u_{i,j}^{n+1} &= u_{i,j}^{n} - \Delta t \cdot \{0.080939[(R' x_{i,j}^{n})] + 0.185235[(R' x_{i,j}^{S})] + 0.185235[(R' x_{i,j}^{2S})] \\
&\quad + 0.154226[(R' x_{i,j}^{3S})] + 0.196431[(R' x_{i,j}^{4S})] + 0.197934[(R' x_{i,j}^{5S})]\}
\end{aligned}
\tag{50}
$$

for x-direction and

$$
\begin{aligned}
u_{i,j}^{S} &= u_{i,j}^{n} - 0.674197\Delta t \cdot [(R' y_{i,j}^{n})] \\
u_{i,j}^{2S} &= u_{i,j}^{n} - 0.674197\Delta t \cdot [(R' y_{i,j}^{S})] \\
u_{i,j}^{3S} &= u_{i,j}^{n} - 0.941974\Delta t \cdot [(R' y_{i,j}^{2S})] \\
u_{i,j}^{4S} &= u_{i,j}^{n} - 0.286400\Delta t \cdot [(R' y_{i,j}^{3S})] \\
u_{i,j}^{5S} &= u_{i,j}^{n} - 0.246018\Delta t \cdot [(R' y_{i,j}^{4S})] \\
u_{i,j}^{n+1} &= u_{i,j}^{n} - \Delta t \cdot \{0.080939[(R' y_{i,j}^{n})] + 0.185235[(R' y_{i,j}^{S})] + 0.185235[(R' y_{i,j}^{2S})] \\
&\quad + 0.154226[(R' y_{i,j}^{3S})] + 0.196431[(R' y_{i,j}^{4S})] + 0.197934[(R' y_{i,j}^{5S})]\}
\end{aligned}
\tag{51}
$$

for y-direction. All of the computational parameters were defined in the previous equations. Using these discretized form of equations, a numerical model is developed to solve domain equations and determine the depth-integrated velocity domain and the water wave surface elevation. The numerical model is verified using several experimental cases. The evaluation of the developed numerical model and comparison of results are discussed in the next sections.

4. COMPARISON WITH THREE-DIMENSIONAL WAVE TANK EXPERIMENTS

A comparison is made with Enet *et al*'s. laboratory data [27], which were obtained in a three-dimensional wave tank for a submerged rigid sliding block. In the experiments, the sliding block

DOI: 10.1002/fld

geometry was defined using truncated hyperbolic secant function as

$$z(x, y) = \frac{T}{r}[\text{sech}(K_w \cdot x) \cdot \text{sech}(K_b \cdot y) - (1 - r)]; \quad \text{for } z \geqslant 0$$
$$K_w = \frac{2}{w} \cdot \text{asech}\left(\frac{1-r}{r}\right) \quad \text{and} \quad K_b = \frac{2}{b} \cdot \text{asech}\left(\frac{1-r}{r}\right) \tag{52}$$

where in the experiments, the truncation ratio; $r = 0.6$, the maximum thickness of slide; $T = 80$ mm, the slide length along the bed slope; $B = 400$ mm, and the slide width; $W = 700$ mm. The parameters are shown in Figure 1. The landslide law of motion is expressed as

$$S(t) = S_0 \cdot \ln\left(\cosh\frac{t}{t_0}\right) \tag{53}$$

where S is the location of centre of sliding mass parallel to the slope and $S_0 = u_t^2/a_0'$ and $t_0 = u_t/a_0'$. u_t is the terminal velocity of sliding solid block and a_0' is its initial acceleration which are defined as

$$u_t = \sqrt{g \cdot B} \cdot \sqrt{\frac{\pi(\gamma - 1)}{2C_\text{d}} \cdot \sin\theta} \quad \text{and} \quad a_0' = g \cdot \frac{\gamma - 1}{\gamma + C_\text{m}} \sin\theta \tag{54}$$

where $\gamma = \rho_\text{l}/\rho_\text{w}$, B is the length of sliding block along the inclined bed, C_d is the drag coefficient, C_m is the added mass coefficient, θ is the bed slope and g is the acceleration due to gravity. ρ_l and ρ_w are the density of landslide and water, respectively. The time-dependent bed geometry is found from the initial geometry as: $\mathbf{x}(t) = \mathbf{x}(0) - S(t)$. $(\mathbf{i} \cdot \cos\theta + \mathbf{k} \cdot \sin\theta)$ where $\mathbf{i}$ and $\mathbf{k}$ denote unit vectors in x- and z-directions, respectively, and $\mathbf{x}$ is the spatial vector of sliding block location in vertical plane (i.e. (x, z)). The surface waves caused by underwater landslide simulated with the present fourth-order model and results compared with experimental data. The comparison is made at two wave gauges located at $x = 0.57$ m, $y = 0$ and $x = 1.498$ m, $y = 0.682$ m. The bed slope is $\theta = 15°$, the sliding block density is $\gamma = 2.7$, the initial submergence of sliding block is $h_{0C} = 0.07$ m, the added mass coefficient is $C_\text{m} = 1.79$ and the drag coefficient is $C_\text{d} = 0.7$ [27], and the initial horizontal location of sliding block is $x_{0C} = 0.57$ m. The dimensions of numerical wave tank are 5.0×4.0 m. The grid size is set to $\Delta x = \Delta y = 10$ cm and the time step is set to $\Delta t = 0.003$ s. The wave pattern obtained from presented numerical model and the locations of wave gauges are demonstrated in Figure 2(a). In this figure, the bed slope of wave tank is truncated at a depth of 1 m. The average values of the experimental data that are obtained from several runs are shown in Figure 2(a). The three-dimensional view of computed impulse wave is shown in Figure 2(b) and the simulated and experimental water surface time series at wave gauges are shown in Figure 2(c). The maximum depression of water surface can be observed in this figure. As seen, an excellent agreement can be observed between presented model and experimental data. The present model accurately simulates the maximum depression of water surface. After passing the main negative wave, the water surface fluctuations are negligible and close to the average values obtained from experimental data. As shown, the present depth-integrated higher-order model can produce an acceptable approximation for the three-dimensional problem.

The numerical results are also compared with experimental data obtained by Grilli *et al*. [28]. All specifications of the problem are presented in Table I. The basic parameters are defined in Figure 1. The location of gauges is mentioned in Table I. The effect of wave propagation on the

DOI: 10.1002/fld

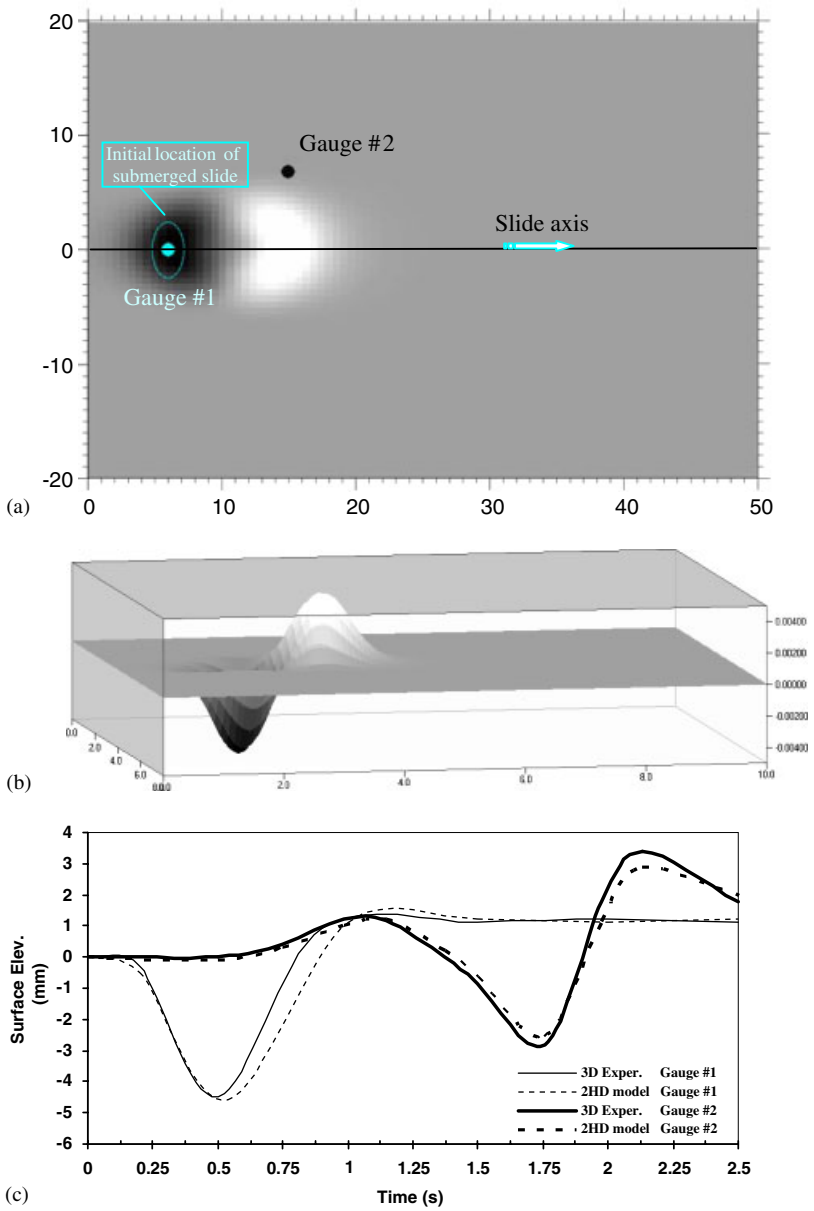

Figure 2. Comparison of the present higher-order model with experimental data at two wave gauges in three-dimensional wave tank, one located at slide axis (Gauge #1; $x = 0.57$ m, $y = 0$) and another located at an arbitrary point (Gauge #2; $x = 1.498$ m, $y = 0.682$ m), the basic parameters are as follows: $\theta = 15°$, $\gamma = 2.7$, $h_{0C} = 0.07$ m, $C_m = 1.79$, $C_d = 0.7$: (a) plan view of numerical wave tank at time $t = 0.6$ s and location of wave gauges and initial location of slide mass; (b) a three-dimensional view of computed surface elevation at time $t = 0.6$ s; and (c) the time series of surface elevation in both wave gauges.

DOI: 10.1002/fld

Table I. The basic parameters for comparison of presented fourth-order 2HD model with three-dimensional experimental data [28].

Parameter	Description	Value	Unit
θ	Planar bottom slope	15	degree
γ	Sliding block density	1.81	–
B	Length of sliding block along the slope	1000	m
T	Maximum thickness of sliding block	52	m
h_{0C}	Initial still water depth at centre point of sliding block	261	m
C_{m}	Added mass coefficient	1.76	–
C_{d}	Drag coefficient	1.53	–
L_1	The length of horizontal part of numerical wave tank	142.5	m
L	Total length of numerical wave tank	4051	m
x_{0C}	Initial horizontal location of sliding block centre of mass	1025.8	m
x'_{g0}	Horizontal location of wave gauge 'g_0' related to x_{0C}	0	m
x'_{g1}	Horizontal location of wave gauge 'g_1' related to x_{0C}	300	m
x'_{g2}	Horizontal location of wave gauge 'g_2' related to x_{0C}	600	m
x'_{g3}	Horizontal location of wave gauge 'g_3' related to x_{0C}	900	m

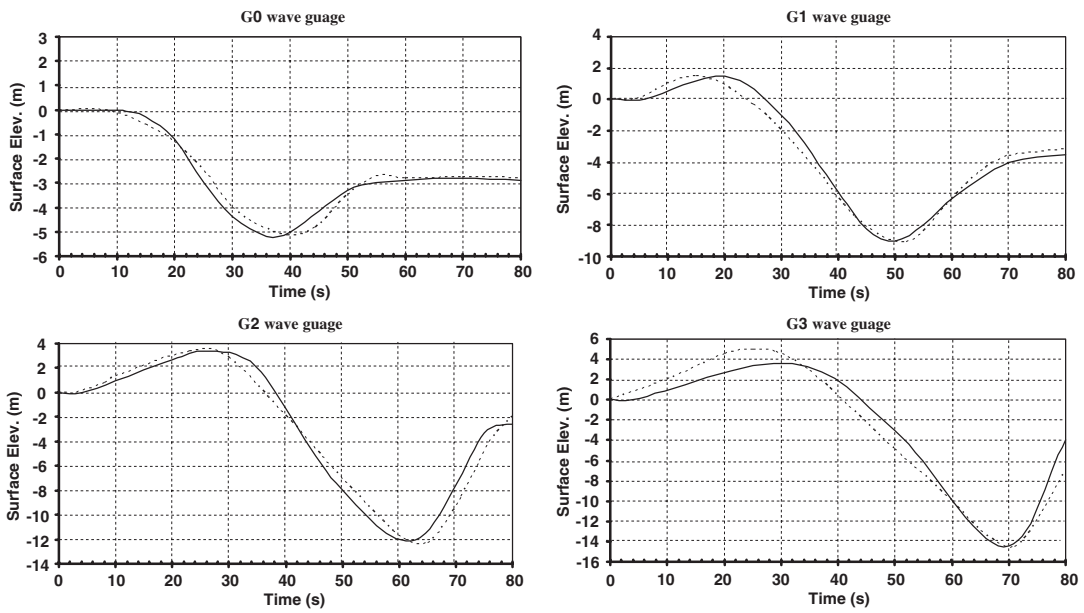

Figure 3. Comparison of the present numerical results (- - -) with the experimental data (—) in four wave gauges G0–G3 located at slide axis, the basic parameters are as follows (scaled up values): $\theta = 15°$, $B = 1000\,\mathrm{m}$, $T = 52\,\mathrm{m}$, $h_{0C} = 261\,\mathrm{m}$, $x_{0C} = 1025.8\,\mathrm{m}$, $\gamma = 1.81$, $C_{\mathrm{d}} = 1.53$, $C_{\mathrm{m}} = 1.76$, $x_{\mathrm{G0}} = 1025.8$, $x_{\mathrm{G1}} = 1325.8$, $x_{\mathrm{G2}} = 1625.8$, $x_{\mathrm{G3}} = 1925.8$.

numerical results is shown in Figure 3. The dimensions of numerical wave tank are $4.5 \times 4.0\,\mathrm{m}$. The grid size is set to $\Delta x = \Delta y = 8\,\mathrm{cm}$ and the time step is set to $\Delta t = 0.0025\,\mathrm{s}$. A good agreement is observed between the present 2HD model and experimental data. As the propagation distance

DOI: 10.1002/fld

increases, the deviation between numerical results and laboratory data increase. Furthermore, the maximum depression of water surface in the initial location of centre of sliding block is accurately simulated. The maximum positive and negative wave heights obtained from the 2HD presented model are close to their experimental values.

5. COMPARISON WITH POTENTIAL FLOW MODELS

In this section, the results of the present depth-integrated fourth-order model are compared with a higher-order boundary element numerical model (BIEM) which developed using fully nonlinear potential theory in a three-dimensional domain [28] and its accuracy in simulating the wave propagation has been well documented [28–30]. First, we compare the present fourth-order depth-integrated model with BIEM results [31, 32]. The geometry of rigid submerged slide mass is different from semi-ellipse shape and is described as a Gaussian shape by [31]

$$z = \frac{T}{1-\psi}\{\mathrm{sech}^2(kx) - \psi\}$$

where

$$k = \frac{2C'}{B} \quad \text{with } C' = \frac{4(\tanh C - \psi)}{\pi(1-\psi)} \quad \text{and} \quad C = \mathrm{acosh}\frac{1}{\sqrt{\psi}} \tag{55}$$

The slide mass length, B, is a function of ψ. Figure 4 shows the different shape of slide mass corresponding to different values of spreading factor $\psi = 0.1$, 0.25, 0.5, and 0.75. As the spreading factor increases, the Gaussian shape is closer to the semi-ellipse geometry that is described by Equation (52) (for two-dimensional slide). The landslide law of motion is the same as Equation (54).

The comparisons are made at two wave gauges and are shown in Figure 5. The time series of water surface elevation at two wave gauges located at $x = x_{0C} = 1.168$ m and $x = 4$ m are shown,

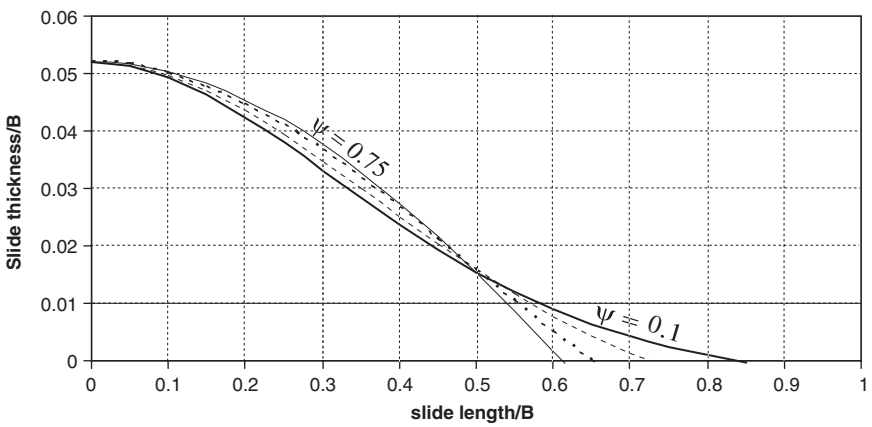

Figure 4. The slide mass geometry based on Gaussian shape (Equation (55)) for different values of spreading factor; $\psi = 0.1$ (—Bold), 0.25 (- - -), 0.5 (- - -Bold), and 0.75 (—), the maximum thickness of landslide; $T = 0.052$ m, and the slide length is $B = 1$ m, the comparison of the present model with BIEM is made based on this geometry [31].

DOI: 10.1002/fld

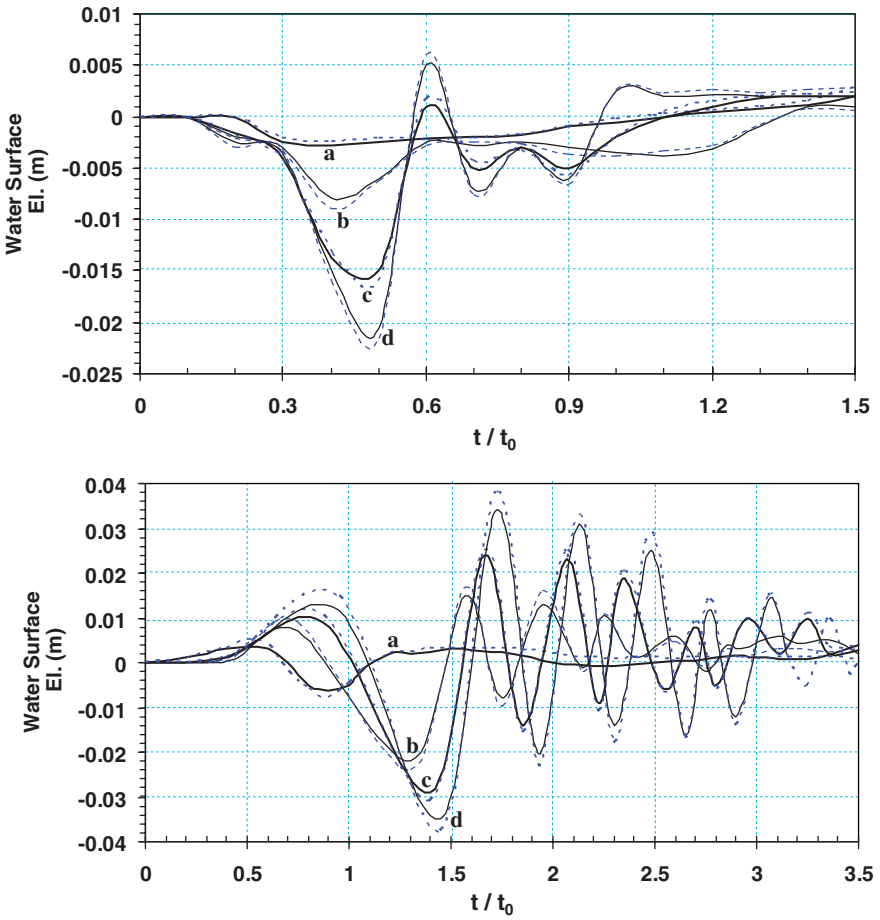

Figure 5. Comparison of the present numerical results (- - -) with BIEM results (—) [31] for time series of water surface elevation at two wave gauges located at $x = x_{0C} = 1.168$ m (top) and $x = 4$ m (bottom), the basic parameters are as follows: $\theta = 15°$, $\gamma = 1.85$, $B = 1$ m, $C_m = C_d = 1$, $T = 0.052$ m, the bed slope truncated at depth $h(x) = 2$ m: (a) $h_{0C} = 0.625$; (b) $h_{0C} = 0.259$; (c) $h_{0C} = 0.175$; and (d) $h_{0C} = 0.125$, the slide law of motion is according to Equation (53) and $t_0 = 2.44$ s, the slide geometry is according to Gaussian shape where $\psi = 0.75$.

for basic parameters are of $\theta = 15°$, $\gamma = 1.85$, $B = 1$ m, $C_m = C_d = 1$, and $T = 0.052$ m. The bed slope truncates at depth $h(x) = 2$ m. The dimensions of numerical wave tank are assumed to be 8.5×5.5 m. The grid sizes, Δx and Δy, are 15 cm and the time step, Δt, is 0.004 s. The results are compared for different values of submergence depth (i.e. h_{0C} in Figure 1) to evaluate the present model accuracy in different conditions. In this comparison, the Gaussian spreading factor, ψ, is 0.75.

As seen, an excellent agreement is achieved in different cases. The maximum depression of water surface and the height of impulsive wave are accurately simulated by the present 2HD model. The deviations of the presented model results from BIEM results increase, by increase in the initial submergence depth of slide mass. The maximum deviation that is occurred at the

DOI: 10.1002/fld

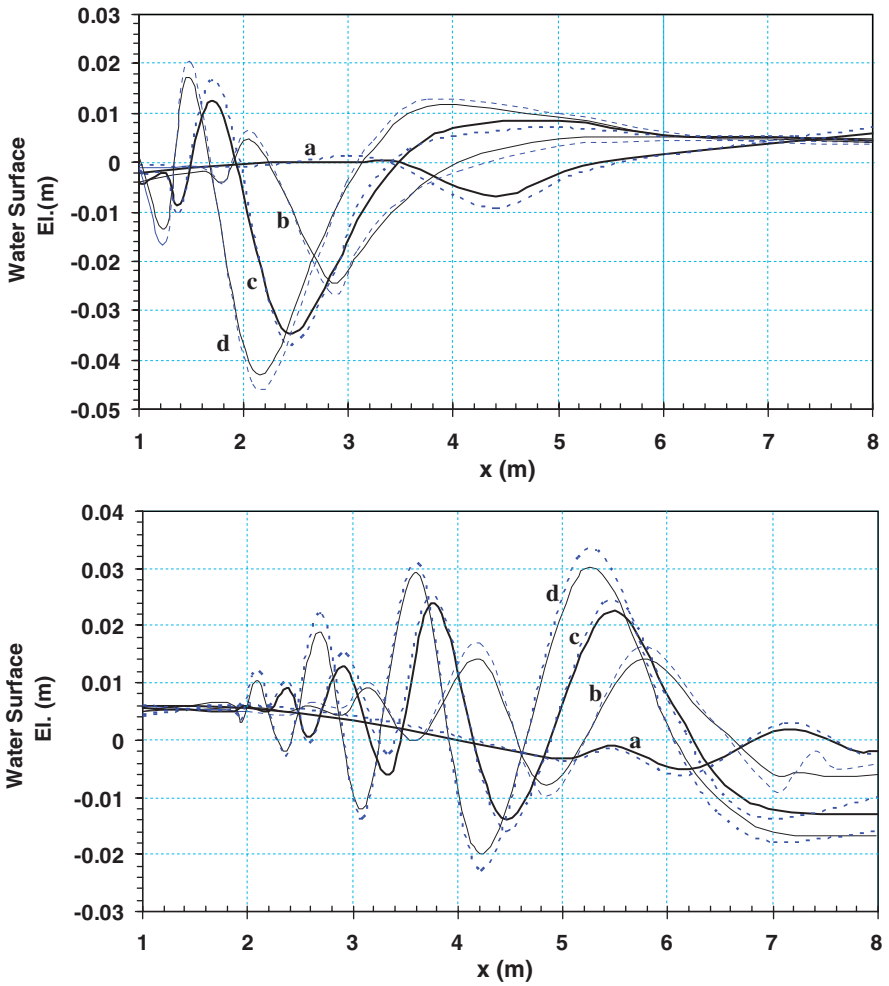

Figure 6. Comparison of the present numerical results (- - -) with BIEM results (—) [31] for water surface profile along the slide axis at time $t = t_0 = 2.44$ s (top), and $t = 2t_0 = 4.88$ s (bottom), all of the basic parameters are the same as described in Figure 5: (a) $h_{0C} = 0.625$; (b) $h_{0C} = 0.259$; (c) $h_{0C} = 0.175$; and (d) $h_{0C} = 0.125$.

maximum water surface fluctuations is less than 5%. The wave height and period at both gauges are accurately simulated in the present model. For further evaluation of the present model, the water surface profiles along the slide axis at two different times $t = t_0$ ($= 2.44$ s) and $t = 2t_0$ ($= 4.88$ s) are shown in Figure 6. The agreement is in an acceptable range, particularly in simulation of maximum water depression and maximum wave height. The observed deviations at the near zone at the upstream of slide zone that are due to the effects of upstream lateral boundary in the present model. The high accuracy of presented depth-integrated model in simulation of wave frequency dispersion is observed in Figures 5 and 6. The present model simulates the wave height after dispersion far from sliding zone accurately. As the submergence depth decreases, the wave height

DOI: 10.1002/fld

and water surface depression increase and the deviation of the present model from BIEM results partially increases. But the deviations are not amplified when the wave propagate away from the slide zone. The maximum deviation from BIEM in the studied cases is limited by 5% both in time series and water surface profile.

6. COMPARISON WITH MULTI-LAYER MODELS

The results of the present model are also compared with the results of a multi-layer high-accuracy model developed by Lynett and Liu [26] which allows for a higher-order accuracy of $O(\mu^2)$ in each layer. The comparison is made in water surface profile along the slide axis and it is considered that the sliding mass is symmetric about the slide axis and the solid sliding block geometry is not changed in width (Y-direction in Figure 1). Four data sets which are compared in this section are as follows: (1) the fully potential theory which is used in BIEM model [28], (2) the one-layer second-order approximation which derived by Lynett and Liu [23], (3) the two-layer approach in which, the order of approximation in each layer is $O(\mu^2)$ [26], and (4) the present fourth-order approximation $O(\mu^4)$. The comparisons of several data sets are made based on the definition of a characteristic water depth ratio as $L_s/h_C(t)$ where L_s is the horizontal length of slide mass and $h_{0C}(t)$ is the submergence of the sliding block centre of mass which can be changed by mass movement. As the slide move into deeper water, h_{0C} increases. The time-variable bottom boundary is defined by [23]

$$h(x,t) = h_0(x) - 0.5T\left[1 + \tanh\left(\frac{x - x_l(t)}{S}\right)\right]\left[1 - \tanh\left(\frac{x - x_r(t)}{S}\right)\right] \tag{56}$$

where

$$\begin{aligned} x_l(t) &= x_c(t) - 0.5T\cos(\theta) \\ x_r(t) &= x_c(t) + 0.5T\cos(\theta) \\ S &= 0.5/\cos(\theta) \end{aligned} \tag{57}$$

$x_l(t)$ and $x_r(t)$ are the location of left-end and right-end points of the solid sliding block. The dimensions of numerical wave tank are 10.5×5.5 m. The grid sizes, Δx, Δy are 15 cm and the time step, Δt, is 0.005 s. The basic parameters are as follows: $\theta = 6°$, $B = 1$ m, $T = 5$ cm, $h_{0C} = 20$ cm, $x_{0C} = 2.37$ m, $\gamma = 1.85$, $C_d = C_m = 1$ and L_s as a horizontal length scale [23] is 3.4 m. Figure 7 shows the comparison of results obtained from four various approaches. Figures 7(a)–(d) show the water surface profile along the slide axis at various times of 1.5, 3, 4.5, and 5.9 s, which are corresponding to dimensionless time, $t \cdot (g/h_{0C})^{0.5}$, of 10.6, 21, 31.6, and 41, and water depth ratios, $L_s/h_C(t)$, of 12.2, 9, 6.2, and 5. Figure 7(e) shows the location of sliding mass at these times and its initial location. The results of all models are reasonable and there is not any major deviation from the fully potential theory. In Figures 7(c) and (d), where the slide mass moves into deeper water, the two horizontal dimensions (2HD) models begin to deviate from BIEM but in both cases, the presented fourth-order model and the two-layer second-order model are in a

DOI: 10.1002/fld

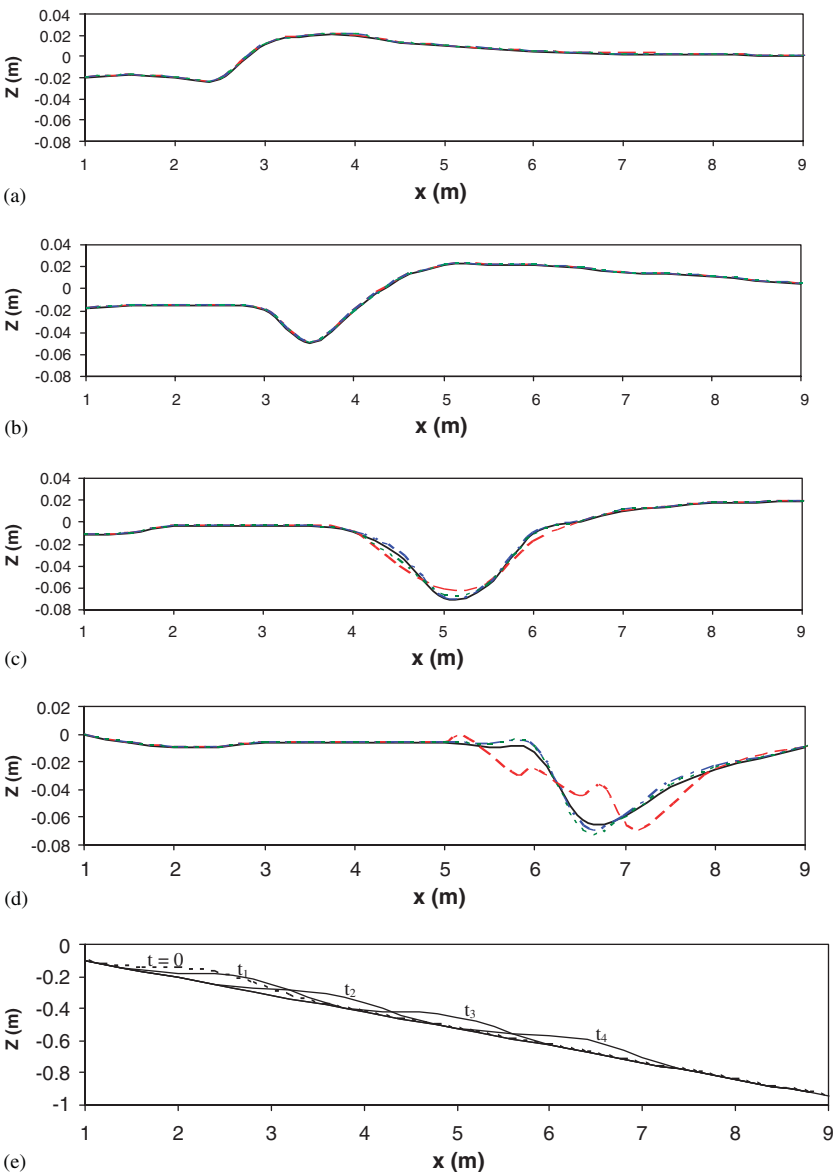

Figure 7. Comparison of the present fourth-order 2HD model (- - -) with BIEM as a potential flow model (—), second-order two-layer 2HD model (- - -) and second-order one-layer 2HD model (- - -), (a)–(d) show the water surface profile along the slide axis at various times: (a) $t_1 = 1.5$ s; (b) $t_2 = 3$ s; (c) $t_3 = 4.5$ s; and (d) $t_4 = 5.9$ s, which are corresponding to dimensionless times: (a) $t \cdot (g/h_{0C})^{0.5} = 10.6$; (b) $t \cdot (g/h_{0C})^{0.5} = 21$; (c) $t \cdot (g/h_{0C})^{0.5} = 31.6$; and (d) $t \cdot (g/h_{0C})^{0.5} = 41$, and water depth ratios: (a) $L_s/h_C(t) = 12.2$; (b) $L_s/h_C(t) = 9$; (c) $L_s/h_C(t) = 6.2$; (d) $L_s/h_C(t) = 5$; and (e) shows the location of sliding mass at various times and its initial location, the basic parameters are as follows: $\theta = 6°$, $B = 1$ m, $T = 5$ cm, $h_{0C} = 20$ cm, $x_{0C} = 2.37$ m, $\gamma = 1.85$, $C_d = C_m = 1$ and L_s as a horizontal length scale [23] is 3.4 m.

DOI: 10.1002/fld

good agreement with BIEM and the one-layer second-order model shows a major deviation from potential theory.

7. COMPARISON WITH LOWER-ORDER APPROXIMATIONS

For a further evaluation, the results of the presented model are compared with the results of a low-order equation set, which describe the impulse wave generation and propagation. For this comparison we used the results presented by Lynett and Liu [23]. The first low-order equation sets consist of fully nonlinear-weakly dispersive equations. Lynett and Liu name this set of equations as fully nonlinear-extended (FNL-EXT) equations that were introduced later as second-order one-layer approximate. The second set of equations is obtained assuming that the thickness of sliding block or the seafloor displacement is relatively small in comparison with the local water depth. The simplified governing equations are called weakly nonlinear-weakly dispersive or extended equations (WNL-EXT). These sets of equations can be simplified into a linear form by neglecting nonlinear terms. Lynett and Liu named this simplified set of equations as linear-extended (L-EXT) equations. Several sets of equations will be compared based on the comparison pattern presented by Lynett and Liu [23]. The basic geometric parameters of each case consist of bed slope; maximum thickness of sliding block and the initial horizontal location of sliding block are presented in Figure 8. The main value used in comparison is the maximum depression of water surface

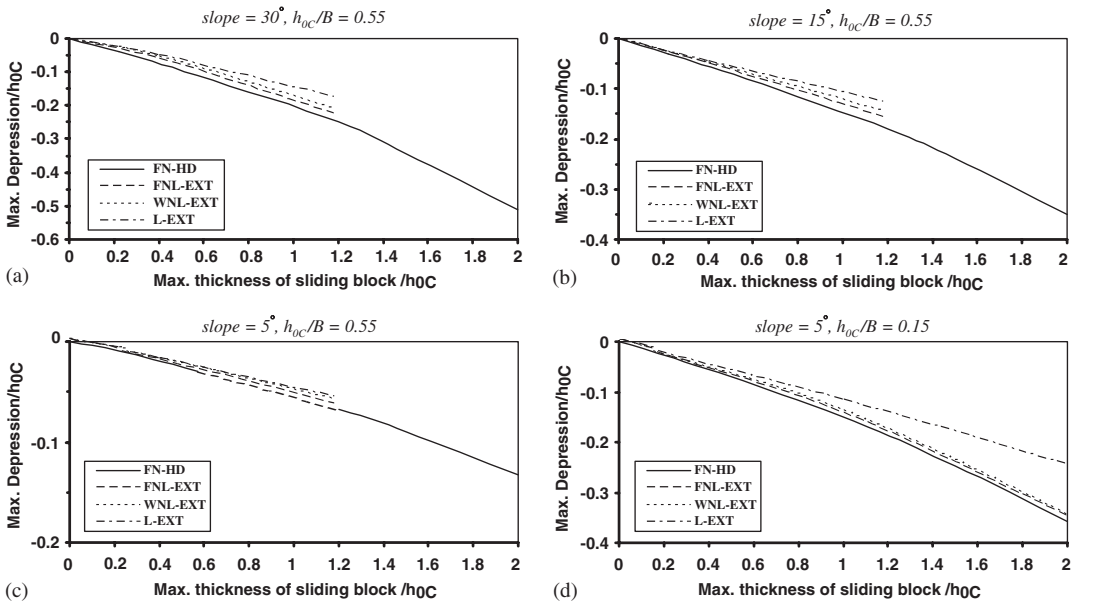

Figure 8. Comparison of presented fourth-order Boussinesq-type model with lower-order approximations in different conditions, all of the parameters are defined in Figure 1, the FN-HD describes the presented higher-order model, the lower-order equations data are obtained from Lynett and Liu comparison [23], all of the models are one-layer, the Lynett and Liu multi-layer approach is discussed in Figure 7.

DOI: 10.1002/fld

elevation at the initial location of sliding block centre. The dimensions of numerical wave tank are 5.0×5.0 m. The grid size is set to $\Delta x = \Delta y = 10$ cm and the time step is set to $\Delta t = 0.002$ s. The effects of nonlinearity and the distinction between equation sets that was used for wave description can be observed in Figure 8. As shown in this figure, the variation of maximum water surface depression using different order equation sets has a similar pattern but in high-order equations this value will be increased. Furthermore, for cases (a), (b) and (c) in the figure, the available data from low-order equations sets consist of FNL-EXT, WNL-EXT and L-EXT have shown a limitation as $T/h_{0C} < 1.2$ where T is the maximum thickness of sliding block. This limitation is not observed in the present fourth-order wave model. Therefore, the superiority of the present higher-order model is shown for steeper beds and for thicker sliding blocks. It must be noted that all of the lower-order approximations described in this section are developed based on one-layer approach. The comparison with multi-layer model was given in the previous section.

8. TEST OF WAVE EVOLUTION OVER SUBMERGED SILL

In this section, the present two horizontal dimensions fourth-order model is checked using a standard test problem [24]. The test problem is related to the passing of a regular wave over an arbitrary fixed bottom in a one-dimensional long flume. The examination of the present model is made by comparing the results with Gobbi *et al.*, one-dimensional fourth-order Boussinesq model [24]. It must be noted that in this case, the bottom is fixed and there is not any landslide or impulse wave. The incident regular wave enters to the flume from left lateral boundary and the wave transition over a submerged sill is investigated. The incident wave and water body characteristics are mentioned in Table II. All of the geometrical conditions of submerged sill and the location of numerical wave gauges as well as the result comparison are shown in Figure 9. The dimensions of numerical wave flume are 1.0 (width) $\times$25.0 (length) m. The grid size is set to $\Delta x = 20$ cm (along the length) and $\Delta y = 10$ cm (along the width) and the time step is set to $\Delta t = 0.004$ s. As it is shown in Figure 9, the present model results are in an excellent agreement with the fourth-order Boussinesq-type model developed by Gobbi and coworkers [24, 25] in one horizontal dimension. The shoaling effects over submerged sill are accurately captured in the present model.

Table II. The incident wave and water body characteristics in formally test of presented fourth-order Boussinesq-type model, the results are compared in Figure 9.

No.	Parameter description	Symbol	Values	Unit
1	Incident wave amplitude	a_0	0.0205	m
2	Incident wave period	T'	1.01	s
3	Incident wave length	L	1.5	m
4	Water depth	h_0	0.40	m
5	Dispersion ratio ($=h_0/l_0$)	μ	0.2666	–
6	Nonlinearity ratio ($=a_0/h_0$)	ε	0.05125	–

DOI: 10.1002/fld

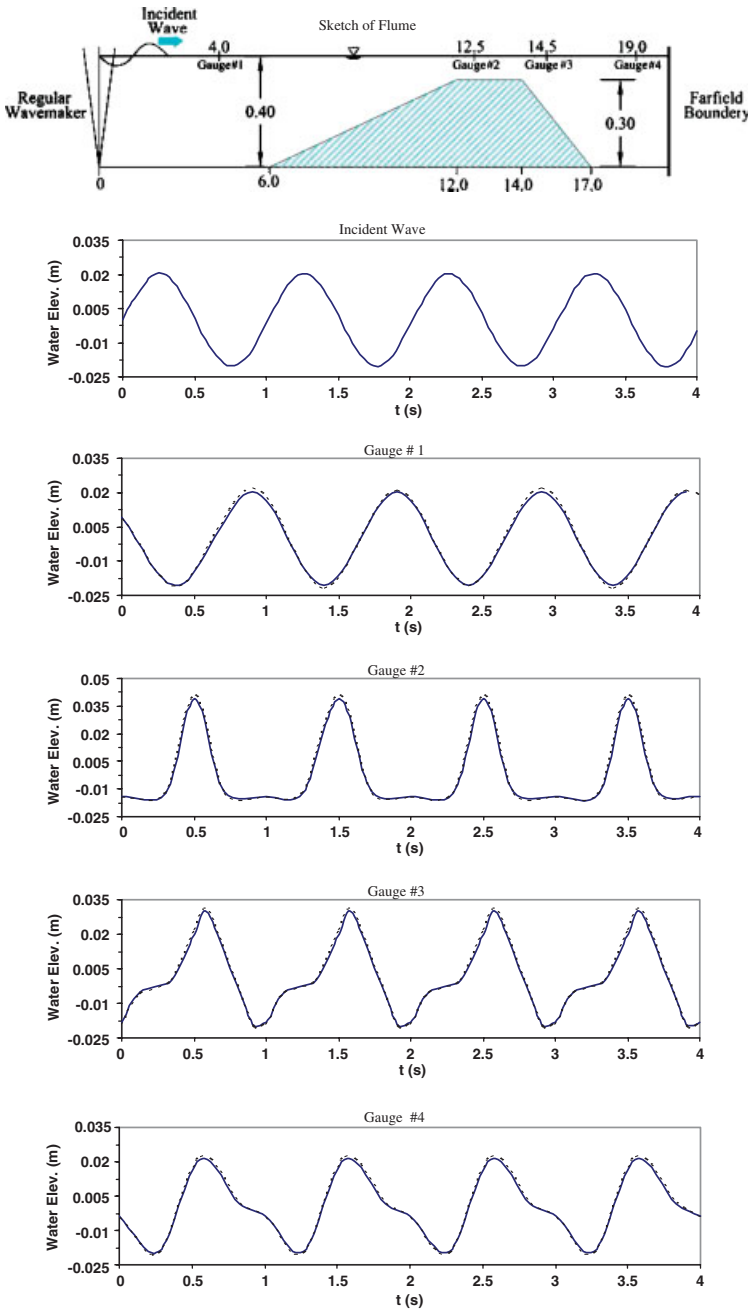

Figure 9. Comparison of presented two horizontal dimension (2HD) fourth-order Boussinesq-type model with Gobbi *et al*., fourth-order one-dimensional model [24] in a regular wave flume with arbitrary fixed bottom, the water surface time series are compared at four numerical wave gauges as a formally check of 2HD presented model.

DOI: 10.1002/fld

9. CONCLUSIONS

A two-dimensional fully nonlinear, higher-order Boussinesq model with moving bottom boundary has been developed in this work. The model retains terms to $O(\mu^4)$, $\mu = h_0/l_0$ in dispersion and to $O(\varepsilon^5)$, $\varepsilon = a_0/h_0$ in nonlinearity where a_0 is characterizes amplitude, l_0 is the characterizes horizontal length scale, and h_0 is the characterizes water depth. The present two horizontal dimensions (2HD) model which can be used for landslide-generated waves is an extension of (4,4) Padé approximant which derived by Gobbi *et al*. [25] for fixed bottom and used in one horizontal direction for investigation of wave propagation over a sill. A depth-integrated numerical model is developed based on derived equations using sixth-order multi-step finite difference method in two horizontal dimensions. The numerical results are compared with three-dimensional wave tank laboratory experimental data [28]. Furthermore, the results of the present two horizontal dimensions model is compared with the results of the three-dimensional fully potential model (BIEM) [31] and a two-layer high-order model [26] and in all cases, an excellent agreement has been achieved. For investigating of the effects of nonlinearity and frequency dispersion, the results are compared with available experimental data at several wave gauges that were installed at different distances from impulse wave source. The comparison shows that the wave height after dispersion, particularly in gauges installed far from the sliding zone are very close to the experimental data. Moreover, the present model checked using a standard test problem of passing a regular wave over an arbitrary fixed sill, and an excellent agreement is also achieved for this case. Thus, the present equations sets show a good agreement with experiments, three-dimensional, and multi-layer models and can be recommended for application for the simulations of the problems of submarine-landslide-generated waves.

NOMENCLATURE

β	the weighting parameter for determination of a characteristic depth (dimensionless)
γ	the water density [$MT^{-2}L^{-2}$]
ε	the nonlinearity ratio $= a_0/h_0$ (dimensionless)
μ	the frequency dispersion ratio $= h_0/l_0$ (dimensionless)
ζ	the water surface displacement from still water level scaled by a_0 (dimensionless)
ψ	the spreading factor for slide mass shape (Equation (43)) (dimensionless)
∇	the horizontal gradient vector $= (\partial/\partial x, \partial/\partial y)$
$\mathbf{A}$	a two-component vector which is used in model derivation (Equation (22a)) (dimensionless)
a_0	the impulse wave amplitude [L]
a_0'	the initial acceleration of slide mass [LT^{-2}]
B	the length of slide mass along the bed slope [L]
C_m	added mass coefficient (dimensionless)
C_d	drag coefficient (dimensionless)
g	acceleration due to gravity [LT^{-2}]
h_0	the characteristic water depth [L]

DOI: 10.1002/fld

$h(x, y, t)$	the depth of moving bottom boundary from still water level scaled by h_0 (dimensionless)
h_{0C}	initial still water depth at centre point of sliding block [L]
L_1	the length of horizontal part of numerical wave tank [L]
L	total length of numerical wave tank [L]
l_0	the horizontal length scale [L]
p	the water pressure scaled by γa_0 (dimensionless)
r	the truncation ratio of hyperbolic secant function (Equation (52)) (dimensionless)
t	dimensionless time scaled by $l_0/(gh_0)^{1/2}$ (dimensionless)
T	the maximum thickness of the slide mass [L]
$\mathbf{u}$	the vector of horizontal velocity components (u, v) scaled by $\varepsilon \cdot (gh_0)^{1/2}$ (dimensionless)
u_t	the terminal velocity of slide mass [LT^{-1}]
$\mathbf{u}_0, \mathbf{u}_1, \mathbf{u}_2$	the dimensionless factors used for expanded form of $\mathbf{u}$ (Equation (10)) (dimensionless)
w	the velocity component in vertical direction scaled by $(\varepsilon/\mu) \cdot (gh_0)^{1/2}$ (dimensionless)
W	the width of slide mass [L]
w_1, w_2	the dimensionless factors used for expanded form of w (Equation (11)) (dimensionless)
x, y	the horizontal coordinates scaled by l_0 (dimensionless)
x_{0C}	initial horizontal location of sliding block centre of mass [L]
$x_l(t)$	the horizontal location of left-end point of the solid sliding block [L]
$x_r(t)$	the horizontal location of right-end point of the solid sliding block [L]
z_a, z_b	the elevations that the horizontal velocity components are described in them, scaled by h_0 (dimensionless)
$\tilde{z}$	the characteristic variable depth which is a weighted average of two distinct water depths, z_a and z_b (dimensionless)
z	the vertical coordinate scaled by h_0 (dimensionless)

APPENDIX A: DERIVATION OF SIXTH-ORDER RUNGE–KUTTA METHOD FOR TEMPORAL DISCRETIZATION

In this appendix, the sixth-order R-K temporal discretization method is presented. The main equation is assumed as

$$\frac{\mathrm{d}u}{\mathrm{d}t} = f(u, t) \tag{A1}$$

where the one-step, six-stage discretization R-K method can be defined as follows:

$$u^S = u^n + \alpha_1 \cdot \Delta t \cdot f(u^n, t^n)$$

$$u^{2S} = u^n + \alpha_2 \cdot \Delta t \cdot f(u^S, t^S), \quad t^S = t^n + \alpha_1 \cdot \Delta t$$

$$u^{3S} = u^n + \alpha_3 \cdot \Delta t \cdot f(u^{2S}, t^{2S}), \quad t^{2S} = t^n + \alpha_2 \cdot \Delta t$$

DOI: 10.1002/fld

$$
\begin{aligned}
u^{4S} &= u^n + \alpha_4 \cdot \Delta t \cdot f(u^{3S}, t^{3S}), \quad t^{3S} = t^n + \alpha_3 \cdot \Delta t \\
u^{5S} &= u^n + \alpha_5 \cdot \Delta t \cdot f(u^{4S}, t^{4S}), \quad t^{4S} = t^n + \alpha_4 \cdot \Delta t \\
u^{n+1} &= u^n + \Delta t \cdot [\alpha_6 f(u^n, t^n) + \alpha_7 f(u^S, t^S) + \alpha_8 f(u^{2S}, t^{2S}) + \alpha_9 f(u^{3S}, t^{3S}) \\
&\quad + \alpha_{10} f(u^{4S}, t^{4S}) + \alpha_{11} f(u^{5S}, t^{5S})]
\end{aligned} \tag{A2}
$$

There are 11 unknown variables which shall be found based on minimization of numerical error. The determination procedure of these variables using Taylor series is explained in the following steps:

$$
\begin{aligned}
f(u^S, t^S) &= f(u^n, t^n) + \sum_{i=1}^{11} \left[\frac{(\alpha_1 \cdot \Delta t)^i}{i!} \cdot \frac{\mathrm{d}^i}{\mathrm{d}t^i} f(u^n, t^n) \right] + o(\Delta t)^{12} \\
f(u^{2S}, t^{2S}) &= f(u^n, t^n) + \sum_{i=1}^{11} \left[\frac{(\alpha_2 \cdot \Delta t)^i}{i!} \cdot \frac{\mathrm{d}^i}{\mathrm{d}t^i} f(u^n, t^n) \right] + o(\Delta t)^{12} \\
f(u^{3S}, t^{3S}) &= f(u^n, t^n) + \sum_{i=1}^{11} \left[\frac{(\alpha_3 \cdot \Delta t)^i}{i!} \cdot \frac{\mathrm{d}^i}{\mathrm{d}t^i} f(u^n, t^n) \right] + o(\Delta t)^{12} \\
f(u^{4S}, t^{4S}) &= f(u^n, t^n) + \sum_{i=1}^{11} \left[\frac{(\alpha_4 \cdot \Delta t)^i}{i!} \cdot \frac{\mathrm{d}^i}{\mathrm{d}t^i} f(u^n, t^n) \right] + o(\Delta t)^{12} \\
f(u^{5S}, t^{5S}) &= f(u^n, t^n) + \sum_{i=1}^{11} \left[\frac{(\alpha_5 \cdot \Delta t)^i}{i!} \cdot \frac{\mathrm{d}^i}{\mathrm{d}t^i} f(u^n, t^n) \right] + o(\Delta t)^{12}
\end{aligned} \tag{A3}
$$

$$
\begin{aligned}
u^{n+1} &= u^n + \sum_{i=1}^{11} \left[\frac{(\Delta t)^i}{i!} \cdot \frac{\mathrm{d}^i}{\mathrm{d}t^i} u^n \right] + o(\Delta t)^{12} \\
&= u^n + \Delta t \cdot f(u^n, t^n) + \sum_{i=2}^{11} \left[\frac{(\Delta t)^i}{i!} \cdot \frac{\mathrm{d}^{i-1}}{\mathrm{d}t^{i-1}} f(u^n, t^n) \right] + o(\Delta t)^{12}
\end{aligned} \tag{A4}
$$

Using the equations in (A2), it can be derived that

$$
\begin{aligned}
\mathrm{Err} = \frac{u^{n+1} - u^n}{\Delta t} &- [\alpha_6 f(u^n, t^n) + \alpha_7 f(u^S, t^S) + \alpha_8 f(u^{2S}, t^{2S}) \\
&+ \alpha_9 f(u^{3S}, t^{3S}) + \alpha_{10} f(u^{4S}, t^{4S}) + \alpha_{11} f(u^{5S}, t^{5S})]
\end{aligned} \tag{A5}
$$

DOI: 10.1002/fld

Substituting $(u^{n+1}-u^n)/\Delta t$ from Equation (A4) and $f(u^{kS},t^{kS})$ $(k=1$ to 5) from Equation (A3) into Equation (A5), the numerical error can be determined as

$$\begin{aligned}\mathrm{Err} = {} & f(u^n,t^n)+\sum_{i=2}^{11}\left[\frac{(\Delta t)^{i-1}}{i!}\cdot\frac{\mathrm{d}^{i-1}}{\mathrm{d}t^{i-1}}f(u^n,t^n)\right]+o(\Delta t)^{11}-\alpha_6 f(u^n,t^n)\\ & -\alpha_7\cdot\left\{f(u^n,t^n)+\sum_{i=1}^{11}\left[\frac{(\alpha_1\cdot\Delta t)^i}{i!}\cdot\frac{\mathrm{d}^i}{\mathrm{d}t^i}f(u^n,t^n)\right]+o(\Delta t)^{12}\right\}\\ & -\alpha_8\cdot\left\{f(u^n,t^n)+\sum_{i=1}^{11}\left[\frac{(\alpha_2\cdot\Delta t)^i}{i!}\cdot\frac{\mathrm{d}^i}{\mathrm{d}t^i}f(u^n,t^n)\right]+o(\Delta t)^{12}\right\}\\ & -\alpha_9\cdot\left\{f(u^n,t^n)+\sum_{i=1}^{11}\left[\frac{(\alpha_3\cdot\Delta t)^i}{i!}\cdot\frac{\mathrm{d}^i}{\mathrm{d}t^i}f(u^n,t^n)\right]+o(\Delta t)^{12}\right\}\\ & -\alpha_{10}\cdot\left\{f(u^n,t^n)+\sum_{i=1}^{11}\left[\frac{(\alpha_4\cdot\Delta t)^i}{i!}\cdot\frac{\mathrm{d}^i}{\mathrm{d}t^i}f(u^n,t^n)\right]+o(\Delta t)^{12}\right\}\\ & -\alpha_{11}\cdot\left\{f(u^n,t^n)+\sum_{i=1}^{11}\left[\frac{(\alpha_5\cdot\Delta t)^i}{i!}\cdot\frac{\mathrm{d}^i}{\mathrm{d}t^i}f(u^n,t^n)\right]+o(\Delta t)^{12}\right\}\end{aligned}\tag{A6}$$

For minimization of numerical errors, the same order terms in Equation (A6) must be equal to zero. This leads to 11 nonlinear equations that can be described as follows:

$$1-\alpha_6-\alpha_7-\alpha_8-\alpha_9-\alpha_{10}-\alpha_{11}=0$$

$$\sum_{n=2}^{11}\left[\frac{1}{n!}-\frac{1}{(n-1)!}(\alpha_1^{(n-1)}\cdot\alpha_7+\alpha_2^{(n-1)}\cdot\alpha_8+\alpha_3^{(n-1)}\cdot\alpha_9+\alpha_4^{(n-1)}\cdot\alpha_{10}+\alpha_5^{(n-1)}\cdot\alpha_{11})\right]=0\tag{A7}$$

Solving the nonlinear equation system (A7) using available numerical methods, the 11 unknown main variables can be determined as

α_1	α_2	α_3	α_4	α_5	α_6	α_7	α_8	α_9	α_{10}	α_{11}
0.674197	0.674197	0.941974	0.286400	0.246018	0.080939	0.185235	0.185235	0.154226	0.196431	0.197934

The above coefficients are substituted in main equation (A2) to conclude the higher-order R-K method. This method is used in temporal discretization of the governing equations in (42), (50) and (51).

ACKNOWLEDGEMENTS

The financial support of Water Resources Management Organization, Ministry of Power of the Islamic Republic of Iran is appreciated (Project number: DAM1-84010). Financial assistance was also provided partly by the Research Office of Sharif University of Technology, Iran.

DOI: 10.1002/fld

REFERENCES

1. Takahashi T, Shuto N, Imamura F, Matsutomi H. The measured and computed Hokkaido Nansei-oki earthquake tsunami of 1993. *24th Conference on Coastal Engineering*, ASCE, New York, 1994; 886–900.
2. Yamashita T, Takabayashi T, Tsuchiya Y. Numerical simulation of tsunami inundation caused by southwest Hokkaido earthquake. *Journal of Japan Society of Civil Engineers* 1994; **41**:231–235.
3. Kennedy AB, Chen Q, Kirby JT, Darlymple RA. Boussenesq modeling of wave transformation, breaking, and run-up. I: 1D. *Journal of Waterway*, *Port*, *Coast and Ocean Engineering* 2000; **126**:39–47.
4. Liu LF, Cho YS, Briggi MJ, Kanoglu U, Synolakis CE. Runup of solitary waves on a circular island. *Journal of Fluid Mechanics* 1995; **302**:259–285.
5. Satu S. Numerical simulation of 1993 southwest Hokkaido earthquake tsunami around Okushiri island. *Journal of Waterway*, *Port*, *Coastal and Ocean Engineering* 1996; **122**:209–215.
6. Titov V, Synolakys CE. Numerical modeling of tidal wave run-up. *Journal of Waterway*, *Port*, *Coast and Ocean Engineering* 1998; **124**(4):157–171.
7. Peregrine DH. Long waves on a beach. *Journal of Fluid Mechanics* 1967; **27**:815–827.
8. Freilich MH, Goza RT. Nonlinear effects on shoaling surface gravity waves. *Philosophical Transactions of the Royal Society of London*, *Series A* 1984; **311**:1–41.
9. Liu LF, Yoon SB, Kirby JT. Nonlinear refraction–diffraction of waves in shallow water. *Journal of Fluid Mechanics* 1985; **153**:153–201.
10. Rygg OB. Nonlinear refraction–diffraction of surface waves in intermediate and shallow water. *Journal of Coastal Engineering* 1988; **12**:191–211.
11. Walkley MA. A numerical method for extended Boussinesq shallow water wave equations. *Ph.D. Thesis*, The University of Leeds, Leeds, U.K., 1999; 70–95.
12. Freilich MH, Guza RT, Elgar DL. Field test of two-dimensional Boussinesq shoaling wave model. *Meeting No. 93-first joint ASCE/ASME/SES Meeting*, 1993.
13. Zhao M, Teng B, Cheng L. A new form of generalized Boussinesq equations for varying water depth. *Journal of Ocean Engineering* 2004; **31**:2047–2072.
14. Abbbot M, McCowan B, Warren IR. Accuracy of short wave numerical model. *Journal of Hydraulic Engineering* 1978; **110**(10):1287–1301.
15. Wu DM, Wu TY, Three-dimensional nonlinear long waves due to moving surface pressure, 14th symposium on naval hydrodynamics. Ann Arbor Mich: National Academy Press, 1983; 103–125.
16. Madsen PA, Sørensen OR. A new form of the Boussinesq equations with improved linear dispersion characteristics. Part 2. A slowly-varying bathymetry. *Journal of Ocean Engineering* 1992; **18**:183–204.
17. Wei G, Kirby JT, Grilli ST, Subramanya R. A fully nonlinear Boussinesq model for surface waves, Part I: highly nonlinear unsteady waves. *Journal of Fluid Mechanics* 1995; **294**:71–92.
18. Madsen PA, Schaffer HA. Higher-order Boussinesq-type equations for surface gravity waves: derivation and analysis. *Philosophical Transactions of the Royal Society of London*, *Series A* 1998; **356**:3123–3184.
19. Chen Q, Kirby JT, Darlymple RA, Kennedy AB, Cawla A. Boussinesq modeling of wave transformation, breaking, and runup. II: 2D. *Journal of Waterway*, *Port*, *Coast and Ocean Engineering* 2000; 48–56.
20. Nwogu O. An alternative form of Boussinesq equations for near shore wave propagation. *Journal of Waterway*, *Port*, *Coast and Ocean Engineering* 1993; **119**(6):618–638.
21. Beji S, Nadaoka K. A formal derivation and numerical modeling of the improved Boussinesq equations for varying depth. *Journal of Ocean Engineering* 1996; **23**:691–704.
22. Li YS, Zhan JM. Boussinesq-type model with boundary-fitted coordinate system. *Journal of Waterway*, *Port*, *Coast and Ocean Engineering* 2001; **127**:152–160.
23. Lynett P, Liu PL. A numerical study of submarine-landslide-generated waves and run-up. *Proceedings of the Royal Society of London*, *Series A* 2002; **458**:2885–2910.
24. Gobbi MF, Kirby JT. Wave evolution over submerged sills: tests of a high-order Boussinesq model. *Journal of Coastal Engineering* 1999; **37**:57–96.
25. Gobbi MF, Kirby JT, Wei G. A fully nonlinear Boussinesq model for surface waves. II. Extension to $O(kh^4)$. *Journal of Fluid Mechanics* 2000; **405**:181–210.
26. Lynett P, Liu PL-F. A multi-layer approach to wave modeling. *Proceedings of the Royal Society of London*, *Series A* 2004; **460**:2637–2669.
27. Enet F, Grilli ST, Watts P. Laboratory experiments for tsunami generated by underwater landslides: comparison with numerical modeling. *Thirteenth International Conference on Offshore and Polar Engineering*, Honolulu, Hawaii, U.S.A., May 2003; 372–379.

DOI: 10.1002/fld

28. Grilli ST, Vogelmann S, Watts P. Development of a 3D numerical wave tank for modeling tsunami generation by under water landslides. *Journal of Engineering Analysis with Boundary Elements* 2002; **26**:301–313.
29. Grilli ST, Watts P. Under water landslide shape, motion, deformation and tsunami generation. *Journal of International Society of Offshore and Polar Engineers* 2003; 364–371 (ISBN 1-880653-5).
30. Grilli ST, Watts P, Kirby JT, Fryer GF, Tappin DR. Landslide tsunami case studies using a Boussinesq model and a fully nonlinear tsunami generation model. *Journal of Natural Hazards and Earth System Sciences* 1999; **3**:391–402.
31. Grilli ST, Watts P. Tsunami generation by submarine mass failure. I. Modeling, experimental validation, and sensitivity analyses. *Journal of Waterway*, *Port*, *Coast and Ocean Engineering* 2005; **131**:283–297.
32. Watts P, Grilli ST, Tappin DR, Fryer GJ. Tsunami generation by submarine mass failure. II. Predictive equations and case studies. *Journal of Waterway*, *Port*, *Coast and Ocean Engineering* 2005; **131**:298–310.
33. Kato K, Tsuji Y. Estimation of fault parameters of the 1993 Hokkaido Nansei-oki earthquake and tsunami characteristics. *Bulletin of Earthquake Research*, vol. 69, University of Tokyo, Japan, 1994; 39–66.
34. Sitanggang KI, Lynett P. Parallel computation of a highly nonlinear Boussinesq equation model through domain decomposition. *International Journal for Numerical Methods in Fluids* 2005; **49**:57–74.
35. Walder JS, Watts P, Sorensen OE, Janssen K. Tsunami generated by sub arial mass flows. *Journal of Geophysical Research* 2003; **108**(B5.2236):EPM 2:1–2:19.
36. Watts P. Wavemaker curves for tsunami generated by underwater landslide. *Journal of Waterway*, *Port*, *Coast and Ocean Engineering* 1998; **12**(3):127–137.
37. Watts P, Grilli ST, Kirby JT, Fryer GF, Tappin DR. Landslide tsunami case studies using a Boussinesq model and a fully nonlinear tsunami generation model. *Journal of Natural Hazards and Earth System Sciences* 2003; **3**:391–402.

DOI: 10.1002/fld